X-Ray Mass and Temperature of Galaxy Clusters

Desiree Della Monica Ferreira
desiree@dark-cosmology.dk

Dark Cosmology Centre - Niels Bohr Institute
University of Copenhagen

Master Thesis
June 2007

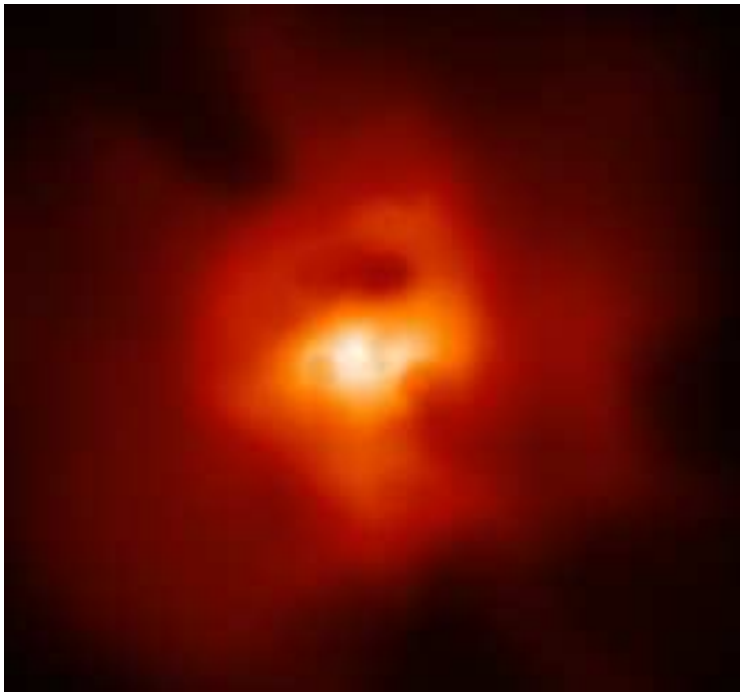

Supervisor: Kristian Pedersen

X-Ray Mass and Temperature of Galaxy Clusters

Master Thesis
Faculty of Science
University of Copenhagen
July 1, 2007

Desiree Della Monica Ferreira
Dark Cosmology Centre - Niels Bohr Institute

Abstract

This thesis presents a study of the relation between the total mass and the temperature of the intra-cluster medium in clusters of galaxies.

Establishing this cluster mass-temperature relation is essential for using clusters to derive cosmological parameters. This relation depends heavily on the assumptions used in deriving the cluster total mass and temperature.

The aim is to test for biases in the mass determination, how they reflect in this mass-temperature relation and determine the scatter of the total cluster mass and the global temperature of the intra-cluster medium derived from X-ray observations.

In this study, the output of cosmological simulations of galaxy clusters were combined to their X-ray emission maps obtained by analyzing virtual X-ray observations of these clusters.

The simulator of the XMM-Newton Observatory, SciSim, was used to perform the virtual observations of four simulated clusters extracted from hydrodynamical simulations.

Each cluster was observed from three orthogonal views, making up 12 data sets.

Using the results from X-ray analysis, the total mass of the clusters and the gas mass were computed, allowing a detailed study of the relation between the cluster mass and temperature.

Acknowledgments

I would like to thank my supervisor Kristian Pedersen for his help in all matters and for his supervision through this work.

I acknowledge the previous work done by Christian Hededal and Jesper Rasmussen on virtual observations of galaxy systems, which was the starting point of my work. I thank Troels Haugbølle for helping me with the temperature maps.

I would like to thank the members of the Dark Cosmology Centre for creating such an inspiring environment where I experience collaboration and friendship.

I wish to thank my co-supervisor Anja Andersen, and my substitute supervisor Darach Watson, for their overall assistance and friendship.

For proofreading part of this work and for suggestions concerning its contents I would like to thank Tamara Davis and Signe Riemer-Sørensen.

I am greatly indebted to Cassia Januario and Sune Hørluck for their friendship and invaluable support throughout the writing process of this thesis.

Finally, I am grateful to Kristian Schaadt for financial support, and to Jesper Stokkendal for making me smile.

Desiree Della Monica Ferreira
Dark Cosmology Centre - Niels Bohr Institute
University of Copenhagen

Copenhagen, June, 2007

Contents

Chapter 1

Introduction

This is the master thesis of Desiree Della Monica Ferreira. The study described herein was carried out from July 2006 to June 2007, under the supervision of Kristian Pedersen.

The aim of this project is to study clusters of galaxies and establish a relation between the cluster total mass and the temperature of the intra-cluster medium.

1.1 Motivation

The use of galaxy clusters as cosmological probes rely on the scaling relations between the total mass and other clusters observables. Uncertainties in these scaling relations are the main source of error in using clusters to derive cosmological parameters [1].

The mass-temperature is a fundamental relation. It connects the properties of the hot gas present in the intra-cluster medium to the total mass of the cluster. The derivation of cosmological parameters rely on this relation to relate the cluster total mass to other cluster observables.

Establishing this cluster mass-temperature relation is essential for using clusters as cosmological probes. Despite the observational effort to measure the mass-temperature, it is still unclear if it scales as predicted.

The aim is to test for biases in this relation and determine the scatter of the total cluster mass and the global temperature of the intra-cluster medium derived from X-ray observations.

1.2 Method

The output of cosmological simulations of galaxy clusters were combined to their X-ray emission maps obtained by analyzing virtual X-ray observations of these clusters.

The simulator of the XMM-Newton Observatory, SciSim, was used to perform the "virtual" observations of simulated galaxy clusters extracted from hydrodynamical simulations. The clusters were chosen based on their masses only. Our sample consists of four galaxy clusters. They have masses $1.3 \times 10^{14} M_{\odot}$, $2.90 \times 10^{14} M_{\odot}$, $2.92 \times 10^{14} M_{\odot}$ and $9.92 \times 10^{14} M_{\odot}$.

Each cluster was observed from three orthogonal views, making up 12 data sets.

The output file from SciSim is of same type as the real XMM-Newton observations which allow for the simulated data the same treatment done to real observations.

The mass-temperature relation depends heavily on the assumptions used in deriving the cluster mass. Using the results from X-ray analysis, the total mass of the clusters and the gas mass were computed, allowing a detailed study of the mass-temperature relation.

1.3 Structure

This thesis is organized in Chapters as follows.

Chapter 1 presents a brief introduction to the main concepts of modern cosmology. It provides the basic information about how we observe and describe the Universe. It introduces the cosmological parameters and scales used in the study these parameters.

Chapter 2 presents a overview of the study of clusters of galaxies and its use as cosmological probes. It introduces the observation of galaxy clusters at different wavelengths. Here the focus is on their X-ray emission and X-ray observables, describing how they connect to provide the cluster total mass and gas mass.

Chapter 3 presents a brief description of X-ray missions and a overview of the XMM-Newton Observatory.

Chapter 4 describes the galaxy clusters used in this study and their virtual observations. It introduces the model adopted in the cosmological simulations, the simulator of the XMM-Newton Observatory, SciSim, and the its setup. Here the steps between the cosmological simulation and the actual virtual observation of the simulated clusters are described.

Chapter 5 describes the data reduction and analysis of XMM-Newton scientific data. The specific XMM-Newton data analysis software, XMMSAS, is introduced, and the extraction of the X-ray images and the spectra is described. The image analysis is performed by fitting of a β model to the X-ray surface brightness profile, and the spectral analysis by fitting of a thermal model to the observed X-ray spectrum.

Chapter 6 presents the results obtained by fitting of a thermal model to the X-ray spectrum of each of the 12 data sets. The methods used in the fit are introduced. The results obtained directly from the cosmological simulations and the results derived from the X-ray analysis are confronted.

Chapter 7 presents the values obtained for the total mass and the gas mass of each cluster, computed by combining the results obtained from the X-ray analysis of each data set. The computed masses are compared to the real masses from the simulations and biases in the methods used to calculate the masses are discussed.

In Chapter 8 the relation between mass and temperature for our cluster sample is discussed and compared to results obtained by previous studies.

Chapter 9 presents summary of this work.

Chapter 2

Cosmology

The purpose of this Chapter is to give a brief overview of the main aspects of modern cosmology providing the basic information and description of cosmological parameters used in this study.

2.1 The large scale Universe

Cosmology is the study of the Universe as a whole. It studies the origin and evolution of the Universe, and its large-scale structures. Cosmologists call large-scale structures objects that are bigger than individual galaxies (scales $\geq 100kpc$)[2].

Cosmology tries to describe the past of our Universe, explain its present and predict its future by creating models that can describe the Universe's behavior.

Modern cosmology is based on the fact that on large scales the Universe appears to be isotropic and homogeneous. The Robertson-Walker metric of space-time describes a universe that is homogeneous and isotropic and is allowed to expand or contract as a function of time. It has the form,

$$ds^2 = -c^2dt^2 + a^2(t)\left[\frac{dr^2}{1-\frac{\kappa r^2}{{R_0}^2}} + r^2\left(d\theta^2 + \sin^2\theta d\phi^2\right)\right] , \tag{2.1}$$

where (r, θ, ϕ) are the space-time co-moving coordinates, t is the proper time, $a(t)$ is the scale factor of expansion or contraction of the Universe with time, κ defines the curvature of the Universe and R_0 defines the curvature radius at the present time. Depending on the geometry of space-time κ can assume different values: $\kappa = 0$ for flat, $\kappa = +1$ for positive curvature and $\kappa = -1$ for a negative curvature.

On large scales gravity is the dominant force. Einstein's theory of general relativity views gravity as a manifestation of the curvature of space-time. The presence of mass-energy curves space-time. Einstein's field equations for a homogeneous and isotropic universe leads to two differential equations relating the scale factor $a(t)$, the energy density $\rho(t)$ and pressure $P(t)$ of the contents of the Universe. These are the Friedmann equation,

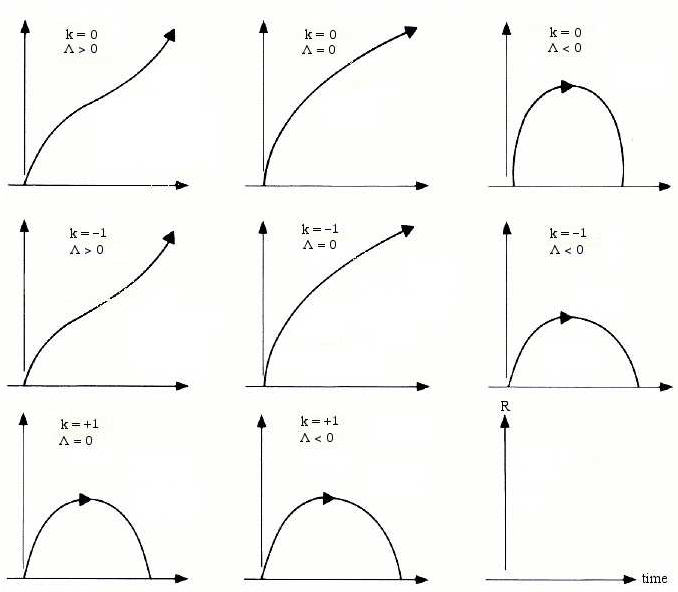

Figure 2.1: Expansion of the Universe as a function of time for different models. Image from James Schombert lecture notes.

$$H^2(t) = \left(\frac{\dot{a}}{a}\right)^2 = \frac{8\pi G}{3}\rho(t) - \frac{\kappa}{R_0^2 a(t)^2} \quad , \tag{2.2}$$

and the fluid equation,

$$\dot{\rho} + 3\left(\frac{\dot{a}}{a}\right)(\rho + P) = 0 \quad . \tag{2.3}$$

These two equations describe the dynamics of the Universe and relate the rate of change in the total energy to the work done by the pressure as the Universe expands. H is known as the Hubble parameter.

Another important relation is the equation of state,

$$P = \omega\rho \quad , \tag{2.4}$$

where ω is a dimensionless number assuming different values depending on the component described. The equation of state of non-relativistic matter has $\omega = 0$, for radiation $\omega = 1/3$ and for dark energy $\omega \leq -1/3$. For the specific case of a cosmological constant, $\omega = -1$. Combining the Friedmann equation, the fluid equation and the equation of state we arrive at the acceleration equation,

$$\frac{\ddot{a}}{a} = -\frac{4\pi G}{3}\left(\rho + 3P\right) \quad , \tag{2.5}$$

which tells us how the expansion rate of the Universe changes with time.

2.2 What is the Universe made of?

The equation of state makes it clear that the dynamics of the Universe are closely connected to what it is made of. Different components have different equations of state and the combined result defines how the Universe evolves.

The directly observable Universe is made of baryons (protons and neutrons), leptons (electrons and neutrinos) and photons. On large scales the Universe is electrically neutral so the number of protons and electrons should be approximately the same. Because protons and neutrons have masses so much larger then the electrons the non-relativistic component of the Universe is often referred to as baryonic matter (even though it also includes electrons) [2].

The two dominant components of the Universe are matter and dark energy. The matter component is made of baryonic matter and non-baryonic dark matter. Dark energy is a mysterious component of the Universe whose pressure is currently causing the expansion of the Universe to accelerate [3]. Another currently negligible component is radiation, made up of photons and neutrinos.

2.3 Cosmological parameters

To describe the many components of the Universe we write the total energy density as the sum of the different components,

$$\rho = \sum_{w} \rho_w \quad . \tag{2.6}$$

It is also convenient to introduce the dimensionless density parameter,

$$\Omega\left(t\right) \equiv \frac{\rho\left(t\right)}{\rho_c\left(t\right)} \quad , \tag{2.7}$$

where $\rho_c\left(t\right)$ is the critical density of the Universe given by,

$$\rho_c\left(t\right) = \frac{3}{8\pi G} H\left(t\right)^2 \quad . \tag{2.8}$$

The Friedmannn equation written in terms of the density parameter takes the form,

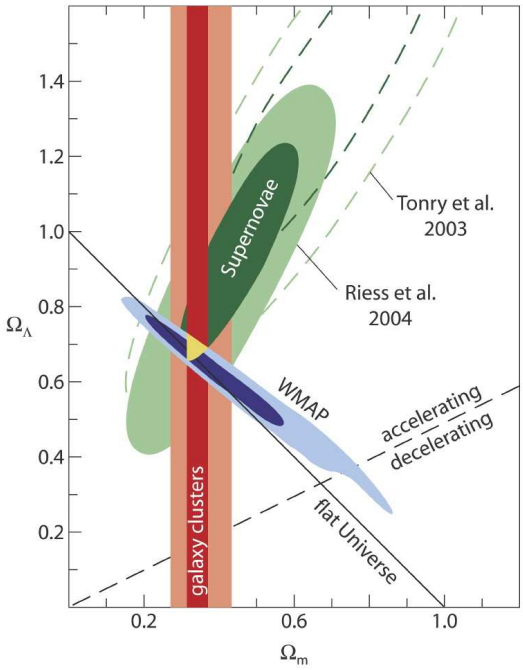

Figure 2.2: Constraints on cosmological parameters derived from different methods. Image from ESO.

$$1 - \Omega(t) = -\frac{\kappa}{R_0^2 a(t)^2 H(t)^2} \quad . \tag{2.9}$$

If we have the energy density of the Universe equal to the critical density so that the left hand side of Equation 2.9 equals to zero, the only solution is a universe with a flat geometry i.e., $\kappa = 0$. In this way, knowing what the Universe is made of also provides information about its geometry and vice versa. We need to find out what the energy density of each component is to put together a model that describes our Universe.

The density parameter of radiation, Ω_{Rad}, is calculated from the cosmic microwave background temperature and Hubble's constant, while many independent studies put constraints on the density parameters of matter, Ω_M, and dark energy, Ω_Λ[3, 4]. Figure 2.2 presents the constrains on cosmological parameters. In this study we discuss the use of galaxy clusters to derive cosmological parameters.

2.4 The ΛCDM model

The ΛCDM model, also referred as the concordance model, is the standard model of Big Bang cosmology. ΛCDM stands for Lambda Cold Dark Matter, and it is the simplest known model for the Universe that is in agreement with the available cosmological observational data. This model considers the Universe as being spatially flat i.e $\Omega = 1$, homogeneous and

isotropic on large scales. It contains radiation, matter (baryonic matter and non-baryonic dark matter) and has a cosmological constant, Λ [5].

The model has six parameters, the density of matter, the density of atoms, the expansion rate of the Universe, the amplitude of the primordial fluctuations, their scale dependence and the optical depth of the Universe. These six parameters are enough to predict not only the statistical properties of the microwave sky but also the large scale distributions of matter and galaxies [5]. This is the model assumed in the cosmological simulations used in this study.

For the ΛCDM model, the values of the density parameter today of total radiation, baryonic matter and non-baryonic dark matter are: $\Omega_R \approx 8.4 \times 10^{-5}$, $\Omega_b \approx 0.04$, $\Omega_{dm} \approx 0.26$, respectively, resulting in a density parameter for the total matter equal to $\Omega_M = 0.30$. The density parameter for the dark energy is equal to $\Omega_\Lambda \approx 0.70$, meaning that our present Universe is dominated by dark energy [2].

The Universe has not always been as we see it today. From the very hot and dense beginning to the quite empty and cool state that we observe today, the Universe went through a radiation dominated phase followed by a matter dominated phase and now appears to have just entered a dark energy dominated phase.

2.5 Distances in the large scale Universe

The cosmologist Edward Hubble made a study relating the redshift of light coming from distant galaxies and their distances. The redshift is defined as,

$$z = \frac{\lambda_{ob} - \lambda_{em}}{\lambda_{em}} \ , \tag{2.10}$$

where λ_{ob} is the wavelength of the light observed after its long journey to us and λ_{em} is the wavelength of the light observed near the place and time of emission [6].

Hubble found a linear relation known today as Hubble's Law. According to the Hubble Law, the velocity of recession of galaxies observed is proportional to their distance from us [2],

$$v_{rec} = H_0 \, d \ . \tag{2.11}$$

For the low redshift case, the Hubble law can be approximated by,

$$z = \frac{H_0}{c} \, d \ , \tag{2.12}$$

where z is the redshift, H_0 is the Hubble constant [1], c is the velocity of light in the vacuum and d is the galaxy's distance from us.

Hubble interpreted the redshift as Doppler shift due to the galaxy's radial velocity moving away from us. If we were able to observe our own galaxy from a distant galaxy we

[1] The best current value of the Hubble constant is $H_0 = 70 \pm 7 kms^{-1}Mpc^{-1}$ [2]

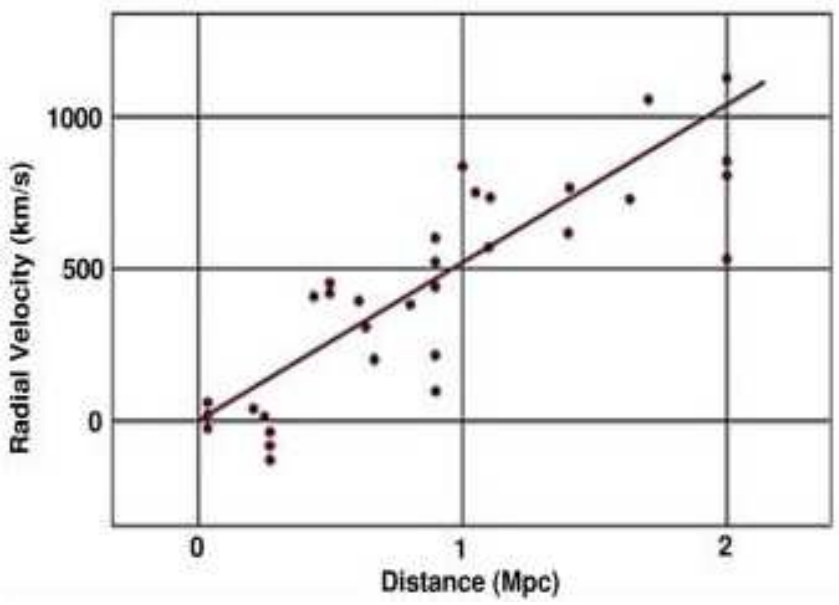

Figure 2.3: Hubble's data of velocity dispersion of galaxies as a function of their distance from us. Image from [7].

would also see our galaxy and other galaxies moving away. This is what we would expect to observe in a universe that is undergoing homogeneous and isotropic expansion[2]. Hubble's study is some of the first observed evidence for the expanding Universe. Figure 2.3 shows Hubble's data.

The redshift is related to the scale factor of the Universe via the equation,

$$1 + z = \frac{a\left(t_{ob}\right)}{a\left(t_{em}\right)} \quad , \tag{2.13}$$

where $a\left(t_{ob}\right) = a_0$ is the scale factor of the Universe at the time the light was observed i.e. the scale factor of the Universe today, and $a\left(t_{em}\right)$ is the scale factor of the Universe at the moment the light was emitted by the source.

The distance d in Equation 2.11 is called proper distance. Unfortunately, the proper distance is not easily obtained from observations. One way of determining how far away an object is becomes possible if the object's luminosity, L, is known. L may be comparable to the object's measured energy flux f. For a flat geometry, the flux f received by a source of luminosity L situated at a distance d_L is given by,

$$f = \frac{L}{4\pi d_L^2} \quad , \tag{2.14}$$

where d_L is called luminosity distance. Equation 2.14 can be written as,

$$d_L = \left(\frac{L}{4\pi f}\right)^{1/2} \quad , \tag{2.15}$$

and d_L can be expressed in terms of redshift by, $d_L = d(1+z)$.

Another possibility for measuring distance comes if the proper length, l, of the object is known. The angle that the object subtends as seen from Earth is related to its distance from us. This relation is called angular diameter distance and for a flat universe it is given by,

$$d_A = \frac{l}{\delta\theta} \tag{2.16}$$

where $\delta\theta$ is the angular extension of the object and $l = a\left(t_{em}\right)\delta\theta d$. Equation 2.16 can be expressed in terms of redshift and related to the luminosity distance by,

$$d_A = \frac{d}{1+z} = \frac{d_L}{\left(1+z\right)^2} \quad . \tag{2.17}$$

2.6 Dark matter

Dark matter is the name given to a component of the Universe that is invisible. The only way we have detected dark matter is by its gravitational effects on visible matter. The dominant type of matter in the Universe is non-baryonic dark matter, which doesn't absorb, emit or scatter light of any wavelength [2].

The first study concerning the existence of large amounts of dark matter was made by Fritz Zwicky in 1930. Studying the Coma galaxy cluster he observed that the dispersion in the radial velocity of the galaxies in the cluster was very large and the gravity provided by the luminous matter in the cluster was not enough to hold the cluster together. Later on with new technology provided by X-ray observatories a large amount of gas was observed in the space between the galaxies but that still couldn't account for the large gravitational potential necessary to keep the system bound [2].

The methods used to detect dark matter are the observation of its effect on the motion of stars and interstellar gas in spiral galaxies, its effect on the motion of galaxies and gas in clusters of galaxies and its effect on the trajectory of photons through acting as a gravitational lens [2].

Understanding how much dark matter is in the Universe and consequently the value of Ω_M is very important for cosmological models and in the determination of the curvature and expansion rate of the Universe. It is also very important for understanding what the Universe is made of [2].

Nobody knows what the dark matter is. There are many dark matter candidates including new elementary particles such as WIMPs and heavy neutrinos, among others.

Currently the more accepted idea is that the dark matter consists of elementary particles produced in the early moments of Big Bang [8].

2.7 Structure Formation

On large scales the Universe is homogeneous and isotropic but on scales of order less than 100 kpc the Universe is full of structures. Such as planets, stars, galaxies and so on.

Looking at how matter is distributed on large scales and at anisotropies in the Cosmic Microwave Background (CMB) are the best ways to learn about evolution of structure in the Universe [8]. Most of the cosmological information extracted from the CMB is obtained through the power spectrum.

The main process for structure formation is gravitational collapse. In this way, dark matter has a crucial role in the formation of structure in the early Universe. The dark energy also also effects the distribution and number density of the large scale structures, because their formation depends on the geometry of the Universe.

The most successful models for the formation of large scale structures assume that the dark matter is a form known as cold dark matter [3]. In the standard cold dark matter cosmological scenario, primordial density fluctuations generated in the early Universe are responsible for structure formation [9]. Density perturbations begin to grow because the gravity of slightly overdense regions attracts matter from neighboring, less dense regions[3].

Studying large scale structures, e.g. galaxy clusters, provides information on the rate of expansion of the Universe, density parameters of matter and the amplitude of primordial fluctuations that are the origin of structure in the Universe [10, 11].

Chapter 3

Clusters of Galaxies

The purpose of this Chapter is to introduce the motivation for studying clusters of galaxies as cosmological probes. It describes what clusters of galaxies are, cluster observations and what the study of X-ray emission from such clusters can provide.

3.1 Introduction

The galaxies in the Universe are not distributed evenly. Surveys of galaxy positions have shown that galaxies are members of larger structures, such as clusters, filaments and voids, which are called large scale structure.

A "cluster of galaxies" is the name given to assemblies of galaxies confined together in a gravitationally bound system, they are the largest objects in the Universe that have reached virial equilibrium. Their masses ranging from $10^{13} M_{\odot}$ for small groups to $10^{15} M_{\odot}$ for the richest ones.

A cluster is said to be either poor or rich, depending on how many galaxies it contains. Clusters are also classified as regular or irregular depending on the overall shape of the cluster [12].

Clusters of galaxies are classified as near or distant according to their redshift. Nearby clusters have redshift $z \leq 0.1$. The most distant cluster found to date has redshift $z = 1.393$ [13].

In this project, four simulated clusters were studied. They are both regular and nearby, with masses ranging from $1.3 \times 10^{14} M_{\odot}$ to $9.9 \times 10^{14} M_{\odot}$.

Galaxy clusters can also be grouped in super clusters. Super clusters can contain one or more clusters. They are systems that are undergoing collapse under their own self-gravity while clusters are fully collapsed objects that have come to equilibrium [2].

Systems like galaxy clusters can provide information for the study of cosmic evolution and structure formation in the Universe [3, 14].

In the cold dark matter cosmological scenario structures like galaxies arise from primordial density fluctuations that grow under the influence of gravity provided by the initial dark matter halos. Low mass objects form first and then merge together to form the large

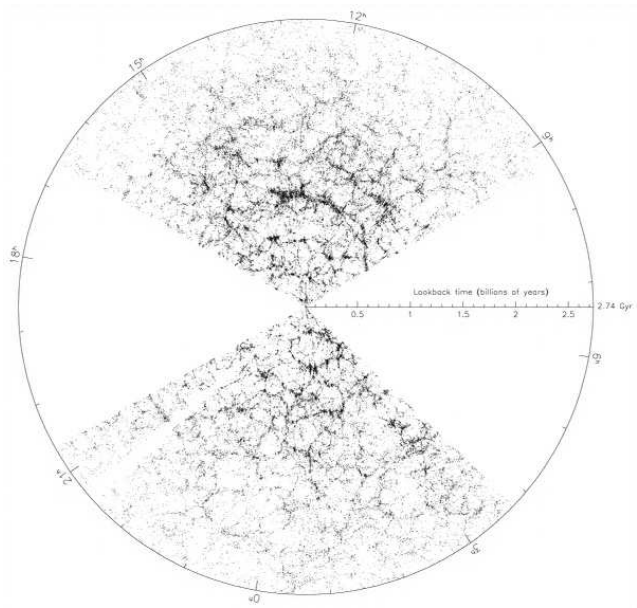

Figure 3.1: Map of the galaxy distribution in the sky. The galaxy clusters appear as the crossing of the filaments, where the galaxies are grouped together. Image from 2dF Galaxy Redshift Survey.

scale structures like clusters of galaxies [8].

3.2 Observing galaxy clusters

Clusters of galaxies were first optically identified by the end of the eighteenth century. As observing power grew, more and more clusters were discovered. In 1958 George Abell published the Abell's catalog containing most of the known nearby galaxy clusters [3].

After identifying the cluster optically, the next step is to obtain the radial velocities of the cluster's galaxies from their redshifts. Zwicky, in 1933, was the first to measure a cluster's velocity dispersion. Extensive redshift measurements also allow observers to study the cluster's mass profile and its dynamical state [3].

The masses of clusters of galaxies can also be measured through gravitational lensing of background galaxies. Lensing is sensitive to the cluster's mass within a given projected radius because the mass within this radius deflects photons toward our line of sight [3, 15].

The light coming from a galaxy behind the cluster is lensed producing multiple distorted images of the original galaxy. Figure 3.2 shows an optical image of Abell 2218 with the lensed background galaxy images distorted into arches.

The stars in clusters of galaxies represent only a small fraction of the cluster's total mass. Clusters contain more mass in the form of hot gas [3]. The intra-cluster medium (ICM), the space between the galaxies inside the cluster, is filled with a low density gas. The gas has temperatures of order 10^7 K. This leads to X-ray emission from processes such as bremsstrahlung.

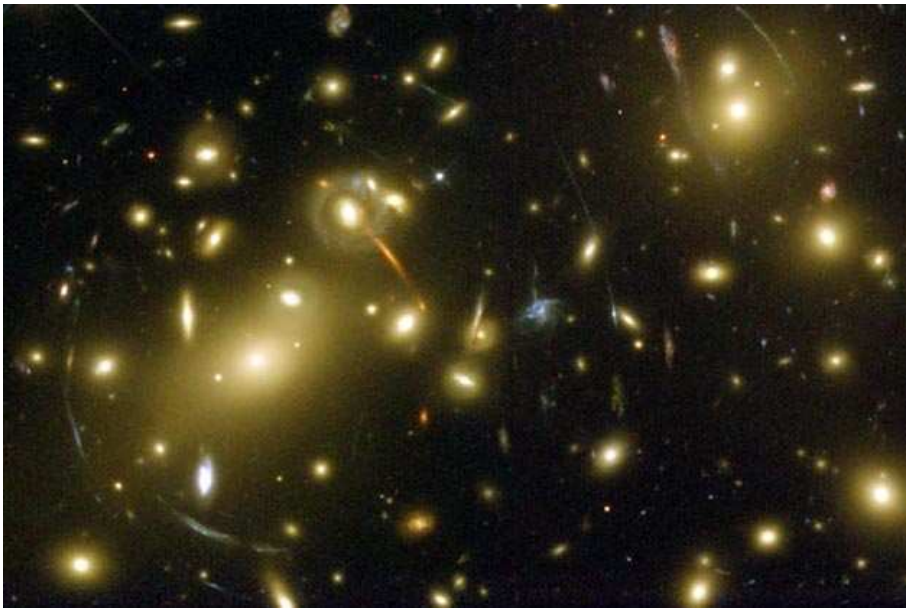

Figure 3.2: Optical image of Abell 2218 with lensed galaxies. Image from NASA

X-ray is the name given to electromagnetic radiation of a wavelength shorter than 10 nm. The X-ray view of galaxy clusters reveals a hot ICM consisting of a hot, tenuous and optically thin gas [9].

Figure 3.3 shows a galaxy cluster in optical and X-ray images. Extended X-ray emission from clusters of galaxies was first observed in the early 1970's [3].

3.3 X-ray properties of galaxy clusters

X-ray emission is expected in sources which contain gas at temperatures in the order of million kelvins, in which the constituents particles have high energy. As the gas cools down it emits X-rays. The emission is a combination of bremsstrahlung and emission lines from highly ionized iron and other heavy elements [2].

Bremsstrahlung is a German word for braking radiation. It refers to the production of radiation by the acceleration of a charged particle when deflected by another charged particle [16]. Therefore, the intensity of bremsstrahlung is proportional to the gas density squared.

Spectral lines are the result of interaction between atoms and photons. Each element has its own characteristic emission and absorption line, therefore, the analysis of line emission from the gas allows the determination of its chemical characteristics [17].

For cluster temperatures $kT \geq 2$ keV, the emissivity of thermal bremsstrahlung dominates that from emission lines, but below 2 keV emission lines dominate.

When we observe galaxy clusters, it is possible to produce an X-ray "image" and also count the number of photons per energy, which is called a "spectrum". From the study of

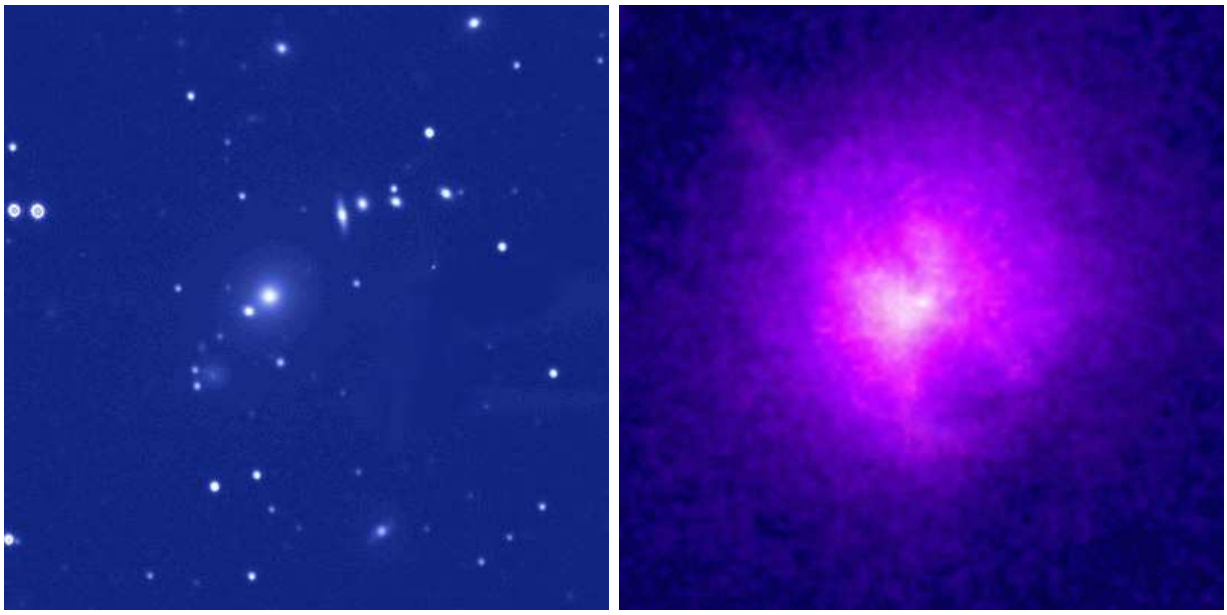

Figure 3.3: The Hydra A cluster of galaxies. Optical image from La Palma B.McNamara (left) and X-ray image from Chandra (right). Images from NASA/CXC/SAO.

X-ray emission from the gas it is possible to derive some of the cluster properties, called here X-ray properties.

Analyzing the X-ray spectrum from clusters makes it possible to fit models for the hot plasma emission and derive the temperature, density and metal abundance of the gas. The X-ray image provides information for deriving the X-ray surface brightness profile, the gas density profile, the cluster's radius and the cluster core.

Combining the results of spectral and image analysis, it is possible to derive the main characteristics of the cluster.

3.3.1 The X-ray Luminosity and Energy Flux

Clusters of galaxies are luminous X-ray sources, with X-ray luminosities ranging from 10^{43} to 10^{46} erg s^{-1} [18].

The luminosity is the amount of energy emitted by a source each second. For clusters of galaxies, the X-ray luminosity is the amount of energy in the form of X-rays emitted by the gas each second.

The X-ray luminosity is calculated from the observed flux in the instrument's energy band. The flux is the energy received per unit of area of the detector each second, or in other words, it is the luminosity per unit area. The emission of electromagnetic radiation has intensity and wavelengths related to its temperature.

The energy flux and X-ray luminosity of clusters are computed by fitting a model to the observed X-ray spectrum for a given redshift and energy range.

3.3.2 Hydrostatic equilibrium and the total cluster mass

The gas in a cluster is trapped by the cluster's gravitational potential well. If the hot gas is supported by its own pressure against gravitational infall, it must obey the equation of hydrostatic equilibrium [2]. In most clusters, the intra-cluster gas appears to be in approximate hydrostatic equilibrium [3]. Assuming spherical symmetry,

$$\frac{d\,P}{d\,r} = -\frac{G\,M(r)\,\rho_{gas}(r)}{r^2} \quad , \tag{3.1}$$

where P is the pressure of the gas, G is the gravitation constant, ρ is the density of the gas and M is the total mass inside the sphere of radius r.

The ideal gas law, $P\,V = N\,k\,T$, that can be written as,

$$P = \frac{\rho_{gas}\,k\,T}{\mu\,m_p} \quad , \tag{3.2}$$

where k is the Boltzmann constant, T is the temperature of the gas, μ is the mean molecular weight of the gas and m_p is the proton mass.

Combining equation 3.1 and equation 3.2, the total mass of the cluster as a function of the projected radius is,

$$M_T(r) = -\frac{kT(r)r}{G\mu m_p}\left(\frac{d\ \ln\ \rho_{gas}}{d\ \ln\ r} + \frac{d\ \ln\ T}{d\ \ln\ r}\right) \quad . \tag{3.3}$$

Assuming an isothermal, spherical gas cloud, with temperature T, equation 3.3 becomes,

$$M_T = -\frac{k\,T\,R}{G\,\mu\,m_p}\left(\frac{d\ \ln\ \rho_{gas}}{d\ \ln\ r}\right) \quad , \tag{3.4}$$

where R is the outer radius of the cluster and μ is constant with radius, since the chemical composition of the gas is expected to be uniform throughout the cluster.

In this project we computed the total masses of four galaxy clusters by assuming spherical symmetry and hydrostatic equilibrium. The results are presented in Chapter 8.

3.3.3 The gas density profile

Assuming an isothermal spherical gas cloud in hydrostatic equilibrium and assuming the volume density of galaxies follows a so called King profile [19], the density profile of X-ray emitting gas can be approximated by an isothermal β model [20],

$$\rho_{gas}(r) = \rho_0\left(1 + \left(\frac{r}{R_c}\right)^2\right)^{-\frac{3}{2}\beta} \quad , \tag{3.5}$$

where $\rho_{gas}(r)$ is the density of the gas as a function of the cluster's projected radius r, R_c is the core radius and ρ_0 is the density at the cluster's center.

The values of β and R_c are obtained by analysis of the X-ray surface brightness profile.

3.3.4 X-ray surface brightness profile

X-ray image analysis allow the determination of the X-ray surface brightness profile. Assuming that the hot gas is isothermal leads to a β model for the cluster's brightness profile,

$$S(r) = S_0 \left(1 + \left(\frac{r}{R_c} \right)^2 \right)^{-3\beta+\frac{1}{2}} + C \quad , \tag{3.6}$$

where $S(r)$ is the X-ray brightness as a function of the projected cluster's radius r. S_0, R_c, β and C, are free parameters in fitting the model to the X-ray brightness profile. In general the X-ray surface brightness profile is well approximated by the β model.

There are cases where the standard β model underestimates the brightness in the central region of the clusters. The central X-ray excess is one of the first pieces of evidence of cooling flows in galaxy clusters [21]. Variations of the original β model have been proposed, e.g., a double β model with a power law component to account for the brighter center [22]. For simplicity, in this study we use a single β model.

In this study, the X-ray surface brightness profile of each cluster in our sample and the fitted β model were obtained from the X-ray images. The results are presented in Chapter 6.

3.3.5 The gas mass

The mass of the hot gas present in the ICM is determined by the integration of the gas density profile, given by equation 3.5, over the volume of the cluster within a defined radius R_{cl},

$$M_{gas} = \int_{cl} \rho \ dV \quad . \tag{3.7}$$

Equation 3.7 can be written as,

$$M_{gas} = 4\pi\rho_0 \int_0^{R_{cl}} r^2 \left(1 + \left(\frac{r}{R_c} \right)^2 \right)^{-\frac{3}{2}\beta} dr \quad . \tag{3.8}$$

The value of ρ_0 is derived from combining the results obtained from fitting a model to the X-ray spectrum, and from the best fit parameters obtained by fitting a β model to the X-ray surface brightness profile. The result obtained by integrating the density profile over a defined volume of the cluster depends on the cosmology assumed because the projected radius of the cluster is calculated using the cluster's angular distance d_A [23].

In this project the gas mass of the clusters in our sample were calculated. The results are presented in Chapter 8.

3.3.6 Temperature of the intra-cluster medium (ICM)

The temperature of the ICM is closely related to the depth of the cluster's potential well. The gas trapped by a cluster's potential well presents temperatures of the order of 10^7 K.

The average temperature T of the gas is derived by fitting a model to the observed X-ray spectrum. The average temperature is a free parameter of the model that is varied to produce the best fit to the observed spectrum.

The assumption of isothermality of the intra-cluster medium is not always valid as some clusters can host cool cores. The result of a cluster's average temperature including cool cores will be lower than the average temperature excluding a core region. We are interested in the average temperature of gas that is relaxed and in hydrostatic equilibrium. That is not the case of a core region hosting cooling flows. Studies of temperature profiles in clusters also show that the temperature generally declines outside the central regions but [24] shows that despite these variations a single integrated temperature, excluding the core regions, remains a good approximation for the total mass.

An isothermal model was fitted to the X-ray spectra of the clusters observed in this project. The results are presented in Chapter 7.

3.3.7 Metal abundance

The metal abundance can be determined from the emission lines of heavy elements in the spectra. A emission line is a bright line in a continuous spectrum resulting from an excess of photons. Emission lines are very specific for each element and can be used to identify the chemical composition of the gas.

X-ray spectroscopy is a powerful tool for analyzing the metal abundance of the ICM. Studies of the chemical abundances of nearby clusters yield a typical mean value for the metallicity in clusters of approximately 0.3 $Z_\odot$ [14], where $Z_\odot$ represents solar metallicity.

3.4 Detecting clusters in microwaves

Hot gas in clusters can also be observed through its effects on the cosmic microwave background. Sunyaev and Zeldovich predicted that hot gas in clusters of galaxies would produce a distortion in the blackbody spectrum, shifting some of the microwave photons to higher energies because of Compton scattering as photons pass through the hot intergalactic gas. The effect is known as Sunyaev-Zeldovich (S-Z) effect [3].

A S-Z survey would measure a distortion parameter Y given by,

$$Y = \int y dA \propto \int n_e T dV \quad , \tag{3.9}$$

where the first integral is over the cluster's surface area and the second over the volume of the cluster. T is the temperature of the gas and n_e the number density of electrons. The y parameter is given by,

$$y = \int \frac{kT}{m_e c^2} n_e \sigma_T dl, \tag{3.10}$$

where k is the Boltzmann constant, m_e is the electron mass, σ_T is the Thomson cross-section and the integral is over the line of sight through the cluster.

The observable Y parameter tells us the total thermal energy of the electrons and can be used as a measure of the cluster mass, once the relationship between the mass and Y has been calibrated [3, 25, 26].

The observation of S-Z effect is independent of the clusters distance unlike the X-rays that lose energy on the way to us. The S-Z effect observations are promising for detecting clusters at high redshift [14, 27].

3.5 Clusters of galaxies as cosmological probes

Clusters of galaxies are probes of structure formation. The evolution of the dark components of the Universe, dark matter and dark energy, is thought to be reflected in the evolution of cluster properties [3, 28, 29]. The use of clusters of galaxies as cosmological probes is based on the assumption that as the largest structures in the Universe that have reached the virial equilibrium they reflect the properties of the Universe itself.

The simplest models of structure formation based on gravitation predict that clusters of galaxies are self-similar [30, 31, 32]. This means that the internal shape of clusters is independent of mass and redshift, and it should be invariant. These theoretical models predict the characteristics and scaling relations of the cluster population and testing these predictions is a challenge for observational cosmology.

Scaling laws relate various cluster properties to each other. They predict how the temperature T relates to the X-ray luminosity L_X, entropy S and total cluster mass M [33, 34].

The standard self-similar model expects a logarithmic slope of $\alpha = 1.5$ for the mass-temperature relation ($M - T$) and $\alpha = 2$ for the luminosity-temperature relation ($L_X - T$) [9].

The $M - T$ is a fundamental relation that connects the properties of the gas to the total mass of the cluster. The derivation of cosmological parameters from clusters of galaxies relies on this relation to relate the cluster total mass to other cluster observables. This relation depends heavily on the assumptions used in deriving the cluster mass profiles [9].

The assumption of hydrostatic equilibrium used to compute the cluster's mass requires measurements of the density and temperature gradients of the ICM, but it is weakened for disturbed clusters. To derive the cluster mass from observable properties such as average temperature and luminosity, it is necessary that the relation between those observables and the total mass is calibrated.

Observations have found the the scaling relations predicted by the self-similar model exist, but they don't reproduce the predictions precisely, e.g., the slope observed for $L_X - T$

is steeper than the one predicted by the standard self-similar model [35, 36], indicating that non-gravitational processes could play a role [32].

Furthermore, a low scatter in the determination of these scaling relations is desirable. The $L_X - T$ relation has a large intrinsic scatter [37, 38], while the $M - T$ relation presents a considerably smaller scatter [39, 40, 41, 26].

The standard self-similar model also predicts the evolution of cluster properties. More distant clusters should be denser, smaller and more luminous [42].

3.5.1 Gas mass fraction

With good estimations of the gas mass and the total cluster mas within a defined radius, the gas mass fraction of the cluster can be calculated. It is defined as,

$$f_{gas} = \frac{M_{gas}}{M_T} \quad , \tag{3.11}$$

where M_{gas} is the mass of the gas and M_T is the total mass of the cluster including the gas, the dark matter, the stars, and everything that can possibly be there.

Self-similar models assume the ICM to be an ideal gas evolving in the gravitational potential of the cluster. The gas mass is a constant and self similarity applies to both the baryonic and non-baryonic contents of the cluster.

The gas mass fraction can be used as a cosmological test based on the fact that this quantity should be a constant for a given cluster radius. Therefore, it provides a standard measure, which should be invariant with redshift.

This enables the matter density parameter, Ω_M, to be determined, since it relates the total amount of matter and the amount of baryonic matter in the Universe [18, 43]. In this way, equation 3.11 can be written as,

$$f_{gas} = \frac{M_{gas}}{M_T} = \frac{\Omega_b}{\Omega_M} \quad , \tag{3.12}$$

where Ω_b is the density parameter of baryonic matter in the Universe and Ω_M is the density parameter of the total mass in the Universe.

The study of clusters of galaxies as probes of the existence of dark matter comes from the fact that, being gravitationally bound systems, they must have enough matter to produce gravity to keep the galaxies and the gas in place. Study of rich clusters reveals that if there was no dark matter to produce enough gravity to anchor the gas, the hot gas would have expanded beyond the cluster [2]. Deriving the gas mass fraction put constraints on the amount of dark matter present in a cluster.

Chapter 4

X-ray Observatories

The purpose of this Chapter is to give a very brief introduction to X-ray observations and a description of the XMM-Newton Observatory. A more complete overview of the XMM-Newton Mission can be found in the given references throughout this Chapter.

4.1 Introduction

X-rays are absorbed by the Earth's atmosphere. Therefore X-ray observations are only possible at very high altitudes, onboard balloons, or onboard satellites. The two X-ray observatories onboard satellites currently in operation are the ESA mission, XMM-Newton, and the NASA mission, Chandra.

The two observatories are complementary. Chandra has better spatial resolution and contains one telescope, while XMM-Newton has larger collecting area and contains three telescopes.

These modern X-ray observatories use CCD detectors that are able to read out the position and energy of individual X-ray photons. The X-rays are collected by mirror modules, which are grazing-incident telescopes, and focused in the focal plane equipped with CCD cameras. Figure 4.1 shows the light path in two of the XMM-Newton telescopes with a reflection grating array mounted into the optical path.

Spatially resolved spectroscopy at medium resolution is possible with these modern telescopes in the energy range between 0.3 and 10.0 keV [9].

Modern X-ray observatories have a tremendous impact on the study of galaxy clusters. Today it is possible to map the gas distribution [44] and temperature in nearby clusters as well as derive temperature and mass profiles [42]. It is also possible to measure basic cluster properties for high redshift objects [45] and find and identify new clusters [46].

A new X-ray mission called eROSITA (extended Roentgen Survey with an Imaging Telescope Array) is already accepted and planned to be launched in 2009. The mission eROSITA, will perform the first imaging all-sky survey in the medium energy X-ray range up to 10 keV with an unprecedented spectral and angular resolution.

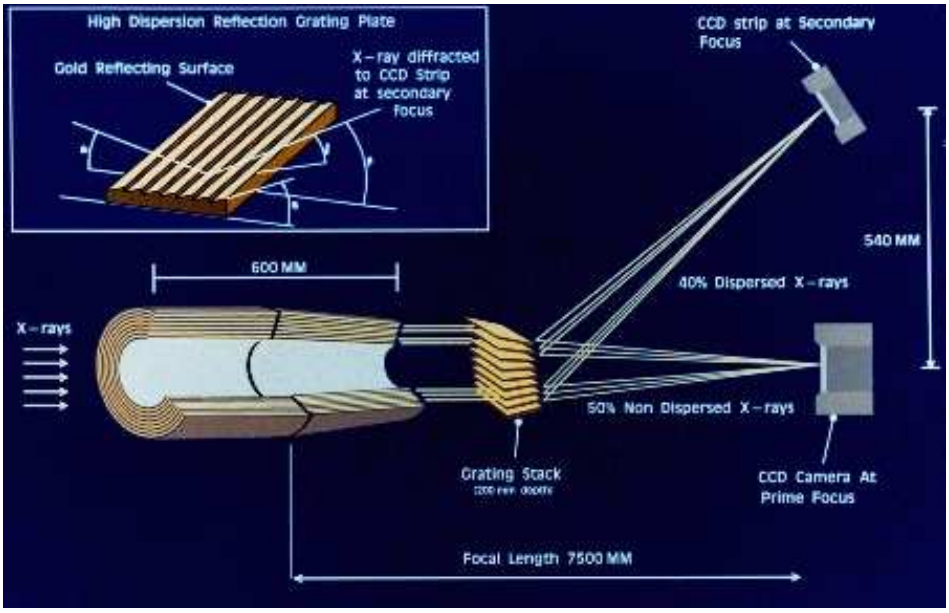

Figure 4.1: Schematic light path for the two XMM-Newton telescopes in which a Reflection Grating Array (RGA) is mounted into the optical path. Image from ESA.

4.2 XMM-Newton

XMM-Newton is is an observatory satellite named in honor to Issac Newton. XMM stands for X-ray Multi Mirror. It is the largest scientific observatory developed by ESA and dedicated to exploring the Universe in the soft-X-ray part of the electromagnetic spectrum [47].

The XMM-Newton ESA mission was launched on December 10th, 1999. It weights 3800 kg and is 10 m long [47]. It is placed in a concentric 48 hour elliptical orbit at 40 degrees. Its apogee is about 114000 km from Earth and its perigee about 7000 km. The attitude and orbit control of the XMM-Newton spacecraft relies on two subsystems on-board: the Attitude and Orbit Control Subsystem (AOCS) and the Reaction Control Subsystem (RCS). Figure 4.2 shows a diagram of the XMM-Newton spacecraft.

It carries two distinct types of telescopes, X-ray and optical/UV, and three types of instruments:

1. European Photon Imaging Camera (EPIC), for X-ray imaging, X-ray spectroscopy and photometry.

2. Reflection Grating Spectrometer (RGS), for high-resolution X-ray spectroscopy and spectro-photometry.

3. Optical Monitor (OM), for optical/UV imaging and spectroscopy.

The basic characteristics of XMM-Newton are: simultaneous operation of all science instruments; high sensitivity; good angular resolution; moderate and high spectral resolution; simultaneous optical/UV observations; and long continuous target visibility. Detailed description the XMM-Newton mission can be found in [47].

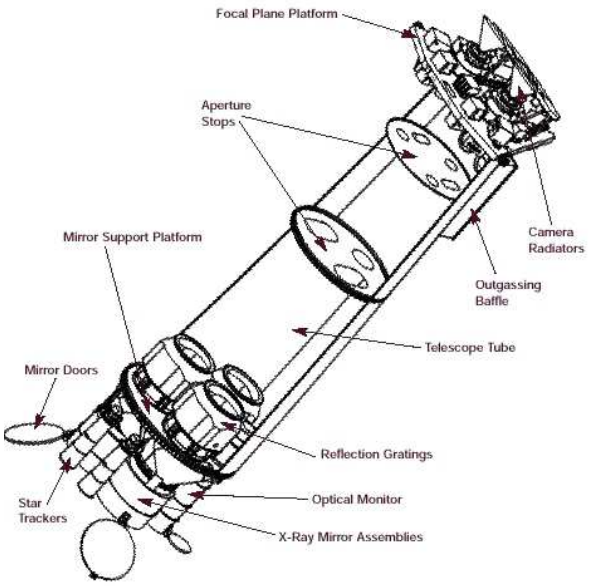

Figure 4.2: Diagram of the XMM-Newton spacecraft. Image from ESA.

The XMM-Newton observatory has three telescopes for collecting X-ray photons. The optics of each telescope consists of 58 nested mirror modules. They are designed to operate in the X-ray energy range of 0.1 to 12.0 keV, with a focal length of 7.5m, and a resolution of 16 arc-seconds. Each mirror module consists of two parts. The front part has a paraboloid surface and the rear part a hyperboloid surface. This configuration allows for double reflection of the grazing X-rays [48]. Figures 4.1 and 4.3 show the optical concept of the XMM-Newton mirror modules.

The EPIC cameras are installed behind the X-ray telescopes and provide extremely sensitive imaging observations. The XMM-Newton telescope carries three EPIC cameras of two different types. Two of the cameras are of the MOS (Metal Oxide Semi-conductor) CCD arrays type. They are both equipped with gratings of the RGS. The third X-ray telescope has an unobstructed beam. The EPIC camera at the focus of this telescope uses pn CCDs.

Each camera has a field of view (FOV) of 30 minutes. The cameras allow several modes of data acquisition, different cameras may operate in different modes. The MOS and pn cameras are fundamentally different. They have different geometry and differ in others properties as well, e.g., their readout time. Figure 4.4 illustrates the layout of the two types of cameras.

All EPIC CCDs operate in photon counting mode producing so called event lists. An event is an X-ray hitting the detector. An event list is a table with the event's attributes, such as position, time and energy, among others [47].

EPIC cameras are not only sensitive to X-ray photons but also to infrared, visible and ultra-violet light. The cameras include blocking filters to reduce the contamination of the X-ray signal by those photons.

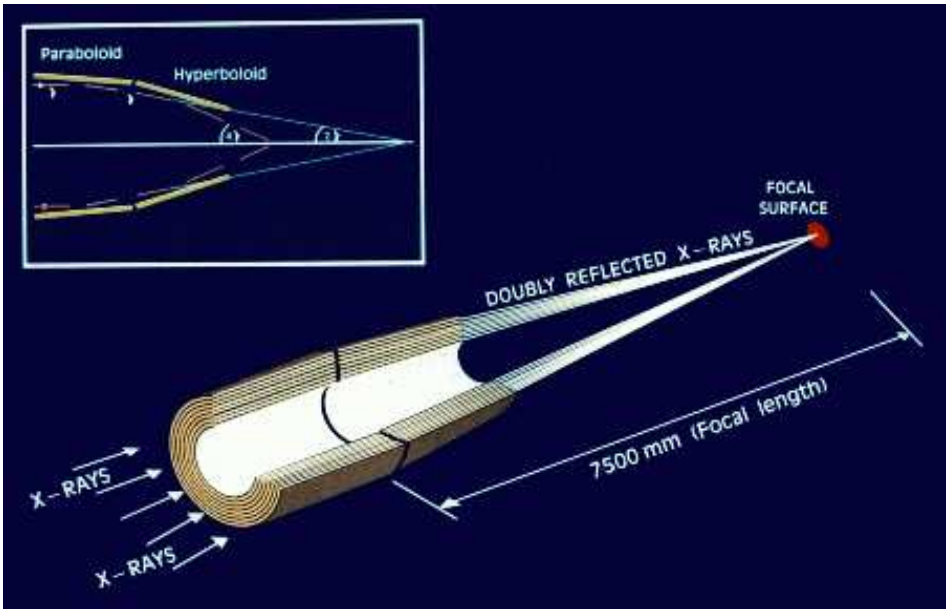

Figure 4.3: Light path in the XMM-Newton telescope with only an EPIC camera (pn) in its primary focus. The other two telescopes (MOS) have a Reflection Grating Array (RGA) in the light path. Image from ESA.

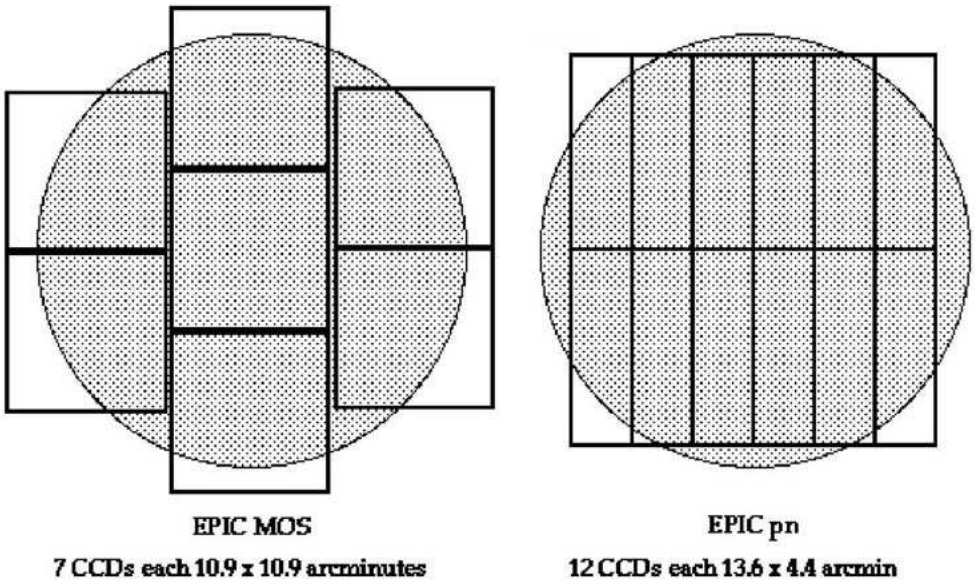

Figure 4.4: Layout of the MOS and pn EPIC cameras. Image from XMM-Newton User's Hand Book.

The presence of background has to be considered too. It can be divided in two categories: a cosmic X-ray background, and an instrumental background. The instrumental background consists of a detector noise component and interaction of particles with the structure surrounding the detectors and with the detectors themselves. The cosmic X-ray background can be an external flaring component but also a stable component due to the interaction of high energy particles with the structure surrounding the detectors and possibly the detectors themselves [48].

The XMM-Newton scientific data is organized in the Observation Data Files (ODF) and Slew Data Files (SDF), most of these files have a FITS format. The ODF/SDF files contain uncalibrated files, which cannot be directly used for scientific analysis. A detailed summary file needs to be created in combination with calibration files to provide information for scientific data analysis [47].

To perform scientific analysis of XMM-Newton data, specific XMM-Newton data analysis software (XMMSAS) is available. The data analysis with XMMSAS performed in this study is described in Chapter 6.

Chapter 5

Simulated Galaxy Clusters

The purpose of this Chapter is to describe the simulated galaxy clusters used in this study and their virtual observations. It provides information about the model adopted in the cosmological simulations, the simulator of the XMM-Newton Observatory and the steps between the output from simulations to input data for observations.

5.1 Cosmological simulations

Cosmological simulations play a important role in theoretical studies of the structure formation in the universe. Simulations are a powerful tool to compute theoretical predictions that can be later compared to observations to understand and describe our universe [49, 50].

Hydrodynamical simulations of galaxy clusters can provide powerful information in calibrating scaling relations between the cluster's X-ray observables and in the understanding of the ICM physics.

5.2 Simulated clusters

The simulated clusters used in this study were extracted from a large cosmological hydrodynamic simulation made by Borgani et al. 2004.

The cosmological model simulated represents a standard flat ΛCDM universe, with matter density $\Omega_m = 0.3$, Hubble constant $H_0 = 70\text{km s}^{-1}\text{ Mpc}^{-1}$, baryon density $\Omega_{bar} = 0.04$ and normalization of the power spectrum $\sigma_8 = 0.8$, which represents the density fluctuations on scales of eight Mpc. It includes radiative cooling assuming zero metallicity, star formation, and supernova feedback [51].

The run used the cosmological simulation code GADGET-2, which is a new version of the cosmological code GADGET. It computes gravitational forces with a hierarchical tree algorithm and represents fluids by means of smoothed particle hydrodynamics (SPH). It can be used to simulate a wide array of astrophysical scenarios, ranging from colliding and merging galaxies, to the formation of large-scale structure in the Universe [52].

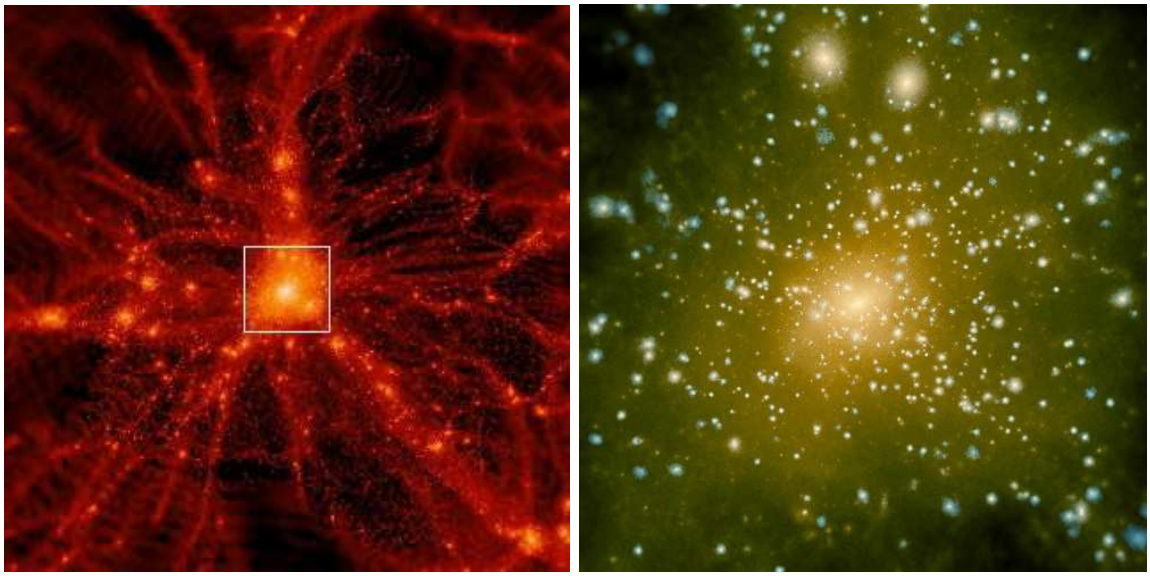

Figure 5.1: Example of a slice through a cosmological simulation box (left), and the region in the white square enlarged, showing a zoom in onto the galaxy cluster (right). Image from Volker Springel.

Neither the development of the cosmological model simulated nor the identification of structures in the output of the cosmological simulation were part of this project.

The large-scale cosmological simulation evolves 480^3 dark matter particles and an equal number of gas particles. Each of the extracted galaxy clusters contains up to 10^6 dark matter particles and 10^5 hot gas particles. A complete description of clusters and groups from this cosmological hydrodynamical simulation is found in [51].

At this point, the first step is to read the information that each particle member of the cluster caries. The output files extracted from the cosmological simulations contain information on clusters having mass M_{500} ranging from $1.3 \times 10^{14} M_{\odot}$ to $9.9 \times 10^{14} M_{\odot}$ at redshift $z = 0$. Where M_{500} is defined as the mass within radius R_{500}, which is the radius enclosing a mean density of 500 times the critical density.

Unlike real observations of clusters, where the cluster mass is not a direct observable, we can obtain from the simulations the correct cluster mass within the defined radius, and later on compare the result obtained from the analysis of the virtual observation.

According to the cosmological model, gas particles above a limiting threshold density are treated as multiphase, composed of a hot, ionized phase and a cold, neutral phase. The ratio between the two phases depends on the temperature and density of the particles [53].

The simulation snapshot for each cluster consists of two files. One contains all the basic information on the simulation and general information on all particles. The other file carries information on the hot and cold phases of the gas separately. Of particular relevance for this project are the density and temperature of the gas particles, which will be used to estimate the X-ray emissivity [53].

The clusters used in this study were selected based on their masses only, in order to

Cluster name	Particles (total)	Gas particles	Star particles	Halo particles
5726	1852486	801841	175682	874963
00010	737962	93371	19946	456113
24174	551670	234927	259987	56756
21926	325153	140861	30385	153907

Table 5.1: Distribution of particles for each of the four clusters.

obtain a representative sample. The particle distribution for each cluster is shown in Table 5.1.

The simulation snapshot contains a three dimensional map with a large number of particles. All particles have individual positions, masses, densities, sizes, metalicities and temperatures. Figure 5.2 presents the two dimensional projection of all cluster particles in three orthogonal views.

Our cluster sample consists of four simulated galaxy clusters with different masses. The cluster 5726 is the most massive one with a mass $M_{500} = 9.91 \times 10^{14} M_{\odot}$. The clusters 00010 and 24174 have similar masses, $M_{500} = 2.92 \times 10^{14} M_{\odot}$ and $M_{500} = 2.90 \times 10^{14} M_{\odot}$ respectively, but differ in the distribution of particles. The cluster 21926 is the least massive one with $M_{500} = 1.30 \times 10^{14} M_{\odot}$. Table 5.2 presents the main characteristics of the clusters.

5.3 Observing simulated galaxy clusters

To observe the simulated clusters in X-rays the software SciSim was used.

SciSim is a simulator for the XMM-Newton X-ray Observatory. It mimics the performance of the XMM-Newton Observatory, by ray tracing incoming photons through the mirror and detector systems. It provides simulated data for a wide range of observational scenarios.

SciSim consists of a number of independent simulators for the different components of the telescope and satellite instruments [54]. These are: Spacecraft Simulator (SPSIM), Mirror Module Simulator (MSIM), European Photon Imaging Camera Simulator (ESIM), Reflection Grating Spectrometer Simulator (RSIM), Reflection Grating Spectrometer Focal Camera Simulator (RFCSIM) and Optical Monitor Simulator (OSIM). There is also the Ray Generator (GSIM) which generates ray tracing data for the X-ray simulators. A detailed description of the simulators is found in [54].

After going through a set of converters, the output file from the simulators are XMM-Newton Observation Data Files (ODFs), equivalent to those obtained from real observations. The ODFs are the final products of SciSim, and are in FITS format.

The steps for setting up a simulation are basically setting up the spacecraft attitude, defining or creating the source field that is going to be observed, configuring the spacecraft, and selecting and configuring the simulators and exposure time.

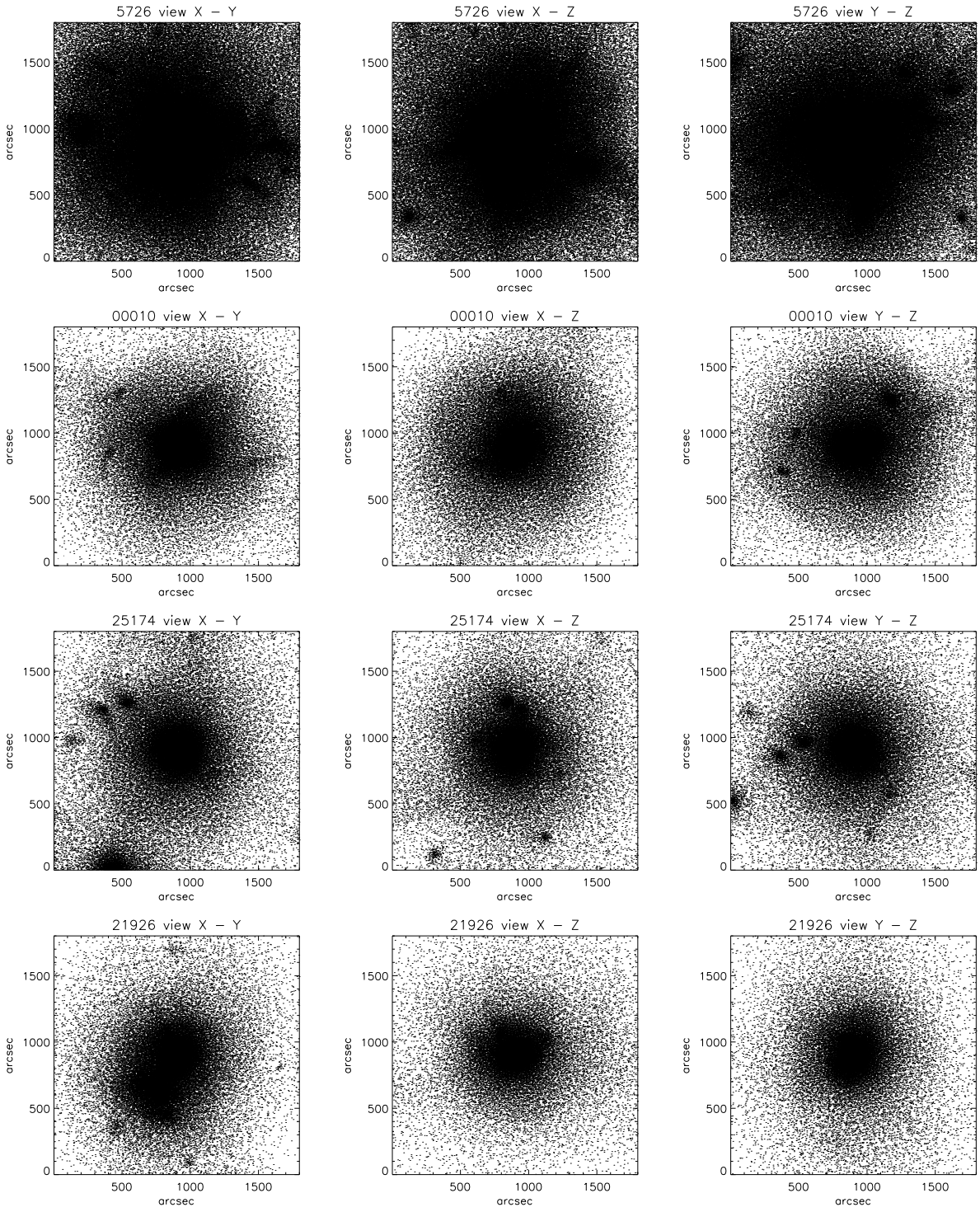

Figure 5.2: Three projected orthogonal views for each cluster including all particles. Starting in the top with the most massive cluster.

Cluster name	R_{500} (kpc)	R_{500} (arcsec)	M_{500} ($M_{\odot}$)	T_{ew} (keV)
5726	1507.35	757.46	9.91×10^{14}	7.25
00010	815.072	409.58	1.92×10^{14}	3.55
24174	869.10	436.73	1.90×10^{14}	2.78
21926	767.94	385.90	1.30×10^{14}	2.51

Table 5.2: Main characteristics of the four clusters extracted directly from the simulation.

SciSim has its own source catalog that can be used for simulating the XMM-Newton observations but manually created sources and simulated sources are also allowed.

Once the source field has been created and the simulators have been configured, the simulation can be executed. When the simulation is complete the result is a binary file that has a SciSim specific format, and contains the results of the exposure as seen by the selected instruments.

The binary file can be converted to an ODF by using the converter `podf`. This command creates a number of FITS files that will later undergo analysis with the XMM-Newton Science Analysis Subsystem (XMMSAS) package.

5.3.1 Creating the source field

Now we want to create a source field containing the cluster to be observed. Our model takes as input a snapshot of a galaxy cluster extracted from a GADGET-2 simulation.

To create a source field from the output file of cosmological simulations, in this case GADGET-2, that can be used by SciSim to simulate the XMM-Newton view of the galaxy clusters, the raw simulated SPH data has to go through some IDL routines to create a list of sources that SciSim can read.

The steps from the cluster simulations to virtual observations are:

1. Read the data from the simulation.
2. Define arrays and XMM-Newton resolution.
3. Calculate the cosmological parameters and distances.
4. Rotate the simulation box which aligns the defined x-axis along the line of sight.
5. Covert positions, selecting only particles that are in the XMM-Newton field of view, given the distance.
6. Discard particles that are outside the energy range of the spectral model MeKal, i.e., below 0.08 keV and above 89.0 keV.
7. Create a spectrum for each gas particle.
8. Move all particles to a XMM-Newton grid.
9. Write all spectra and source files into a file that SciSim can read.

Here a series of IDL procedures were combined to create a pipeline for the procedures above.

When calculating the emitted spectra, the software Xspec was used to assign a MeKaL spectrum to each of the gas particles. Chapter 6 introduces the software Xspec and the model MeKal when describing the spectra analysis.

Given a viewing angle and cosmological redshift, the hot gas particles are projected onto the sky plane along the line of sight. The four clusters were observed at redshift $z = 0.1$. At this redshift three out of the four clusters can be observed out to radius R_{500}.

For the given redshift and cosmology ($\Omega_m = 0.3$, $H_0 = 70$km s^{-1} Mpc^{-1}, $\Omega_{bar} = 0.04$, $\sigma_8 = 0.8$), the clusters luminosity distance is 495.5 Mpc and the angular diameter distance, 1.99 arcsec kpc^{-1}.

Each gas particle is projected onto a source grid of resolution 300×300 with a grid distance of six arcseconds. The result is a two dimensional flux map with energy as a third dimension. The energy interval is limited to 0.5 to 10 keV and a diffuse cosmic X-ray background (CXRB) was added.

5.3.2 Ready to observe

At this point we have a list of sources arranged on a grid to represent the cluster. All these sources are listed in the file `scisimlist.dat` and have their corresponding X-ray spectra.

Given a list of input sources and their spectra, SciSim traces the X-rays through the XMM-Newton Observatory.

SciSim maintains the inclusion of galactic absorption for a given column density. For the observations performed in this study, a galactic column density of $N_H = 5 \times 10^{20}$ cm^{-2} was assumed.

The exposure time, detector and other parameters of SciSim are set in the file `scisim.cfg` which carries all the configuration details of the simulators and exposure time.

In this study, each of the four clusters was observed by the `pn` EPIC camera, with exposure time set to 2.5×10^3 seconds, in each orthogonal view.

The output of SciSim converted into ODFs is now converted into photon event files for each CCD chip of each detector. This is done using the XMMSAS task `odffix`. The next step is to used the XMMSAS task `epchain` to create calibrated event files for each pn CCD chip and merge these into a combined event list. The output file is now ready for the standard scientific analysis of XMM-Newton data.

Chapter 6

Scientific Analysis of XMM-Newton Data

The purpose of this Chapter is to give a overview of the scientific analysis of XMM-Newton data, introducing software and steps of data reduction and analysis.

6.1 XMM Science Analysis System

At this point SciSim has performed the XMM-Newton observation of the four simulated clusters and the output file has gone through converters to generate the FITS files that are ready to undergo scientific analysis.

The XMM Science Analysis System (XMMSAS) is a software package developed to reduce and analyze the XMM-Newton science data. It consists of different tools, and new versions of the software package are released periodically.

In this study we are mainly interested in the XMMSAS tools which: 1. Apply the calibrations to ODF science files producing calibrated events files that can be analyzed; 2. Allow the extraction of light curves, images, spectra, instrument response matrices and source lists [55].

Once the calibrations are applied to the ODF science files they are read for the scientific analysis.

6.2 X-ray image

To extract a X-ray image from the events file the XMMSAS task `xmmselect` was used.

`xmmselect` is a meta-task which allows the creation of filtered event lists, images, histograms, spectra, among other features, from an initial event list data set.

The extracted images are saved as FITS files. The X-ray image is very important in the study of clusters. The first information it provides is the overall condition of the cluster and its morphology.

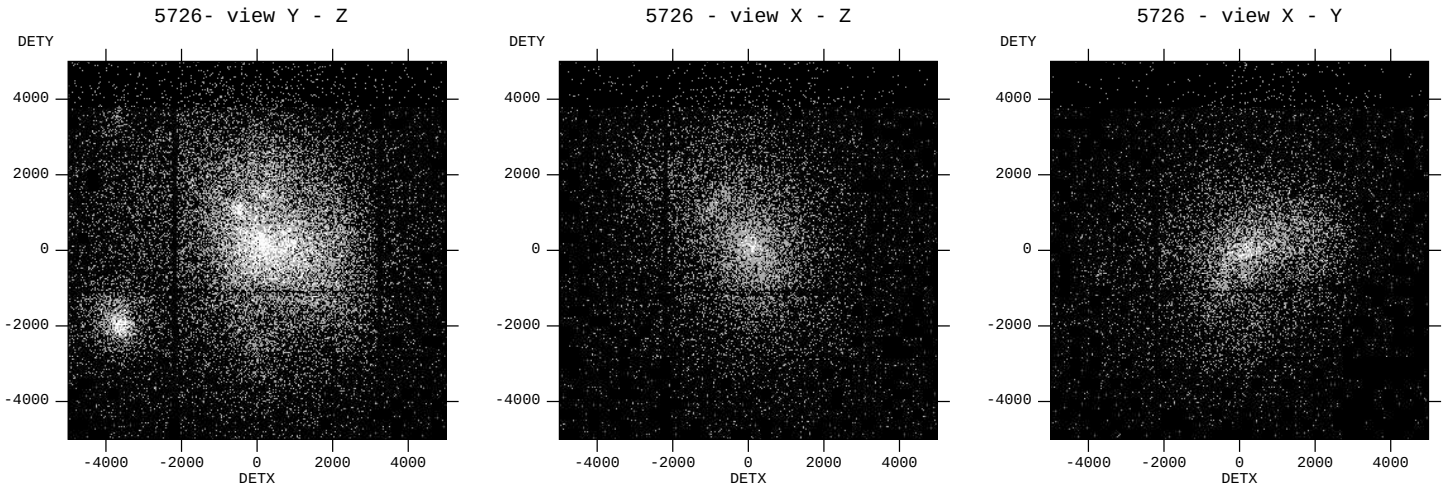

Figure 6.1: X-ray images of the simulated cluster 5726 obtained from the virtual observations. Here in three orthogonal views. For this cluster, it is possible to identify the presence of structures and lack of spherical symmetry.

Spherical symmetry

In this analysis, it is assumed that the clusters are spherically symmetrical. The lack of symmetry will therefore introduce errors in the values obtained for the cluster masses and gas masses.

Unlike real observations, the use of simulated clusters and virtual observations allow the observation of the same cluster in different views. A cluster that from one view appears to be spherically symmetrical may not have the same characteristic when observed from different angles.

In Figure 6.1, the X-ray image of the most massive cluster in our sample is shown. For this cluster we see a clear difference between the three orthogonal views. There are structures and the cluster appears to be elongated, presenting a elliptical shape. The presence of structures and lack of spherical symmetry compromise the agreement between the expected and derived results.

The Figures 6.2, 6.3 and 6.4, show the clusters 00010, 24174 and 21926 respectively, and their three orthogonal views. At first glance, no significant difference between the different views is observed. In principle, these clusters are a good example of spherical symmetry, and this should be reflected in the final results obtained from the X-ray analysis.

Later in this Chapter we discuss the X-ray surface brightness profile, where we see that the clusters are not perfectly symmetric.

Source removal

Once we have the image of the cluster, it is possible to generate region files selecting the areas of the image that should be used. It is possible, for instance, to generate a new image excluding point sources or structures that are not interesting for the further data analysis.

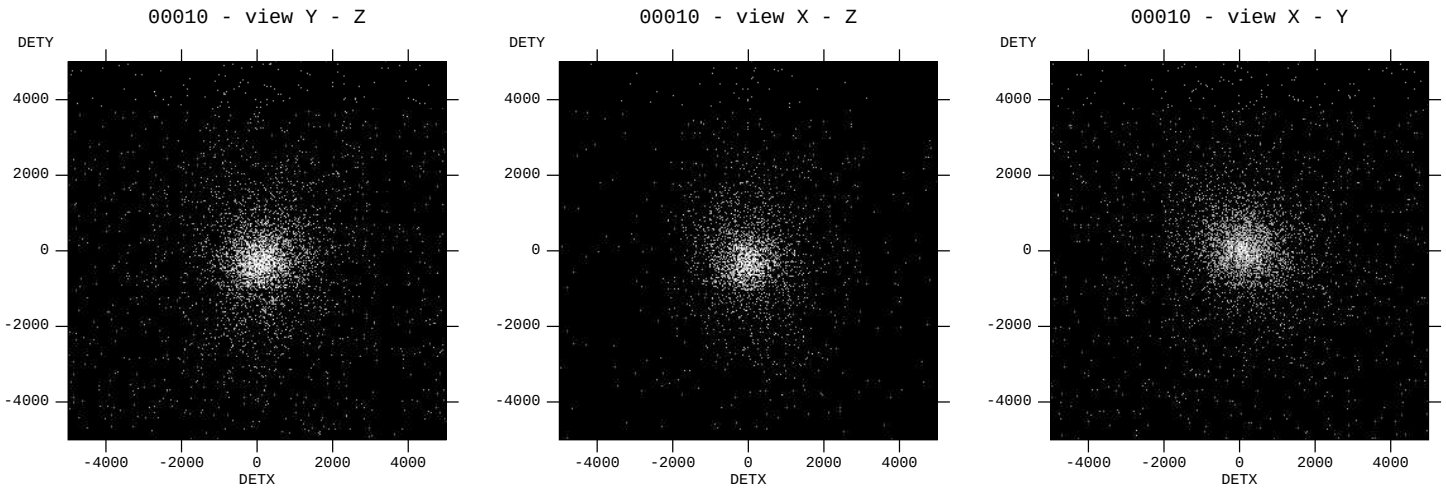

Figure 6.2: X-ray images of cluster 00010 in three orthogonal views.

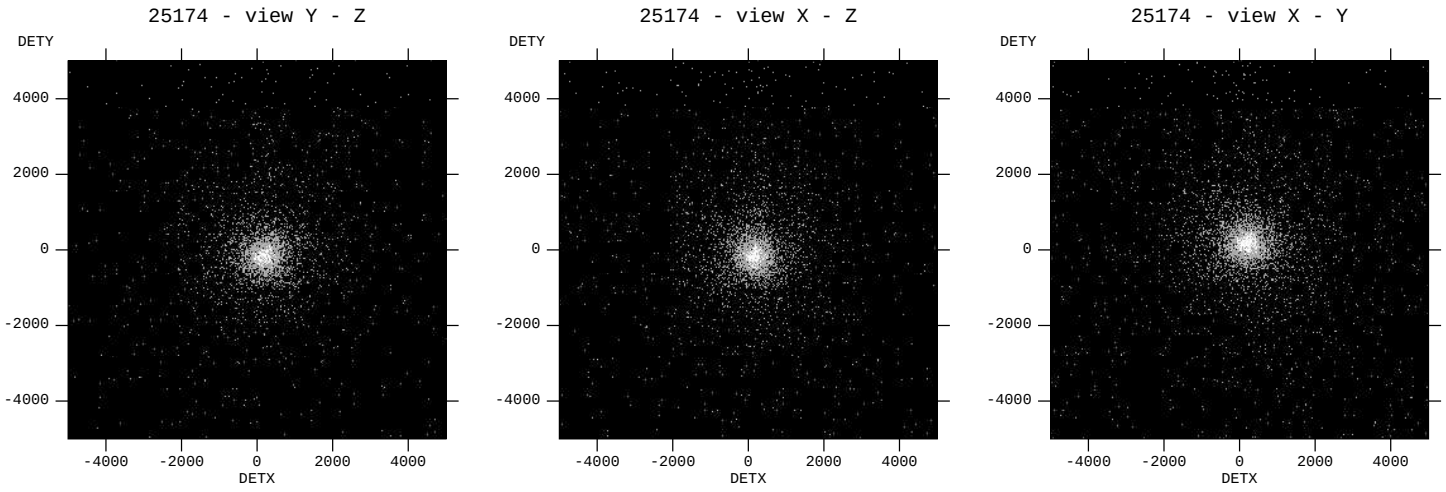

Figure 6.3: X-ray images of cluster 25174 in three orthogonal views.

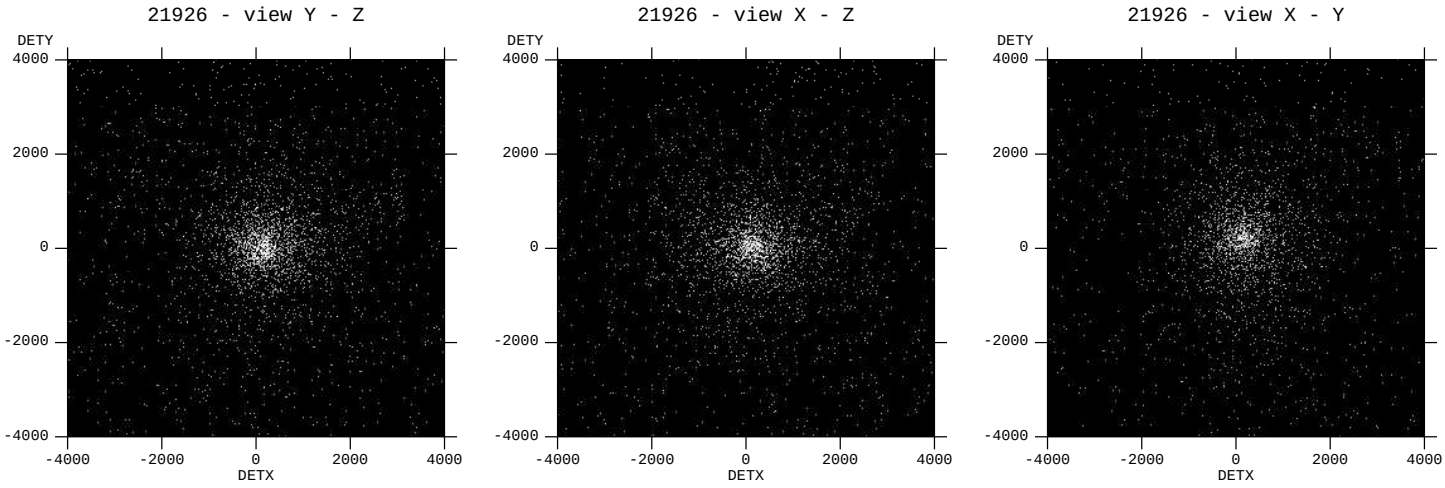

Figure 6.4: X-ray images of cluster 21926 in three orthogonal views.

In Figure 6.8 a example of source removal is shown.

Before the X-ray images extracted with `xmmselect` can be used, they need to be corrected accounting for instrument efficiency. For that we use exposure maps.

Exposure Maps

An exposure map is an image containing the effective exposure time at a given energy band and detector position. It corresponds to a flat field in optical imaging.

An exposure map can be extracted using the XMMSAS task `eexmap`. It uses the calibration data on the spatial quantum efficiency, filter transmission, mirror vignetting, and field of view, to produce instrument maps containing the spatial efficiency of the instrument. From the instrument maps, exposure maps are constructed for a given observation (image).

All images extracted were corrected with the respective exposure map before undergoing further analysis.

Figure 6.5 shows an example of exposure map for the pn EPIC camera.

6.2.1 X-ray surface brightness profile

X-ray imaging observations allow the determination of the X-ray surface brightness profile of the intra-cluster gas.

The first step is to produce and read the X-ray image. We used a IDL program to read the FITS image obtained from the XMMSAS tools. After being read by IDL the resulting image is a matrix 1158x1158 which contains the number of photon counts.

The next step is to find the cluster's center.

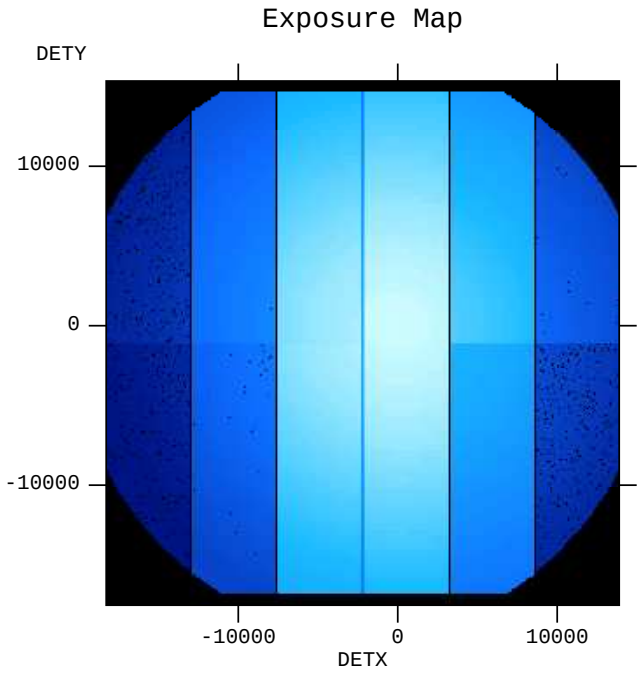

Figure 6.5: Example of exposure map of EPIC pn camera.

Cluster's center

The first use of the X-ray image is to define the center of the galaxy cluster. For that, the image is read into IDL, which understand the image as a matrix with number of counts. A histogram of the number of counts is then produced to decide where the number of counts is the highest in the image. The choice of the cluster's center is important since spherical symmetry is one of our first assumptions in the analysis.

Knowing the coordinates of the cluster's center, annuli are calculated from the cluster's center to the nearest image border. The annuli are equally spaced throughout the projected radius. The number of counts in each annulus gives us the brightness profile.

The β model

The X-ray surface brightness profile obtained from the X-ray image is now modeled with the β model [20], given by Equation 3.6. Fitting the β model to the X-ray surface brightness profile results in the best-fit parameters R_c, β and C.

The accuracy of the β model is very important because the results obtained from fitting this model to the X-ray surface brightness profile will be used to derive the cluster's total mass, via Equation 3.4, and the gas mass, via Equation 3.8.

Many regular clusters have cooling flows which appear as peaks in the X-ray surface brightness profile near the cluster center [56]. This region should be excluded from the fit to the overall profile [57].

For the present cluster sample, modeling the entire profile, including the central part of the cluster, with the β model resulted in a poor fit.

Previous studies show that, even though the β model generally describes the observed X-ray surface brightness profile well, it often underestimates the central surface brightness [21], and tend to overestimates the brightness for projected radius r much larger then R_c [57].

We tried to fit the β model to the entire projected radius. It results in a poor fit. This discrepancy may be due to the fact that the intra-cluster medium is not perfectly isothermal, presenting cooling flows, and with density differing from the proposed King profile [3].

Different fit trials were done to choose the region to be excluded. The radius of the region to be excluded was increased until the quality of the fit was acceptable. We tried to define the same region, proportional to R_{500}, for all clusters. This worked well for three out of four clusters. The most massive cluster had a larger region excluded.

The part outside R_{500} was also excluded. Thus, the fit was done considering the range between $0.025R_{500}$ and R_{500} for three of the clusters, excluding in this way the most inner and outer parts of the cluster. As one example of this, Figure 6.6 presents the X-ray brightness profile of cluster 00010 with the fitted β model.

The radius corresponding to R_{500} for the most massive cluster, 5726, lies outside the field of view of XMM-Newton. For this case we excluded the region within $0.05R_{500}$, and used the region outside this core to fit the data.

This cluster has yet another complication. The presence of structures in the X-ray image image of cluster 5726 creates peaks in the surface brightness profile and compromise the fitting of the model to the data. This is shown in Figure 6.8.

To fix that, a new image is produced excluding the bright structures so that they will not contribute to the brightness profile. All the three orthogonal views of this cluster present structures, and the cleaning procedure was performed for each of the three views.

The image reduction and analysis was performed for each cluster in each of the three orthogonal views. The results of the best-fit parameters are presented in Table 6.1. In the literature, typical values of β are distributed between 0.5 and 0.8 [21]. The results obtained in this study are also in this range.

For a perfectly spherically symmetrical and relaxed cluster, we would expect the X-ray surface brightness profile to be the same in different views. But the presence of structures, asymmetries, and thermal variations, result in differences in the slope of the X-ray brightness profile.

The differences we observe for the different views in our results indicate that the clusters analyzed are not perfectly spherically symmetrical and they probably host cooling flows in their innermost region. These discrepancies in will propagate to the computed values of total cluster mass and gas mass.

A mild trend of β with the cluster temperature has also been reported [21], where hotter clusters would have larger value for β. This result is also reproduced here.

cluster	R_{500} (arcsec)	view	β	Rc (arcsec)
5726	757.46	y - z	0.70 ± 0.05	82.1 ± 2.3
		x - z	0.64 ± 0.03	64.8 ± 1.4
		x - y	0.65 ± 0.04	71.1 ± 2.0
00010	409.58	y - z	0.65 ± 0.01	28.2 ± 0.4
		x - z	0.74 ± 0.05	35.7 ± 0.8
		x - y	0.66 ± 0.02	29.4 ± 0.4
24174	436.73	y - z	0.63 ± 0.01	12.9 ± 0.1
		x - z	0.63 ± 0.01	12.6 ± 0.2
		x - y	0.59 ± 0.01	10.2 ± 0.2
21926	385.90	y - z	0.58 ± 0.02	19.8 ± 0.6
		x - z	0.49 ± 0.02	14.8 ± 0.4
		x - y	0.53 ± 0.03	17.6 ± 0.6

Table 6.1: Result obtained by fitting a β model to the X-ray brightness profile of the four clusters in the three orthogonal views.

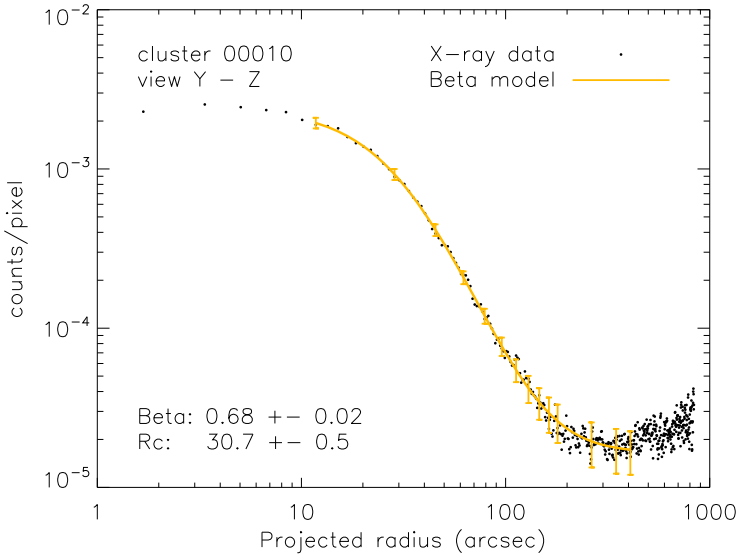

Figure 6.6: X-ray surface brightness profile of cluster 00010 and fitted β model, excluding the innermost part of the cluster and the region outside R_{500}.

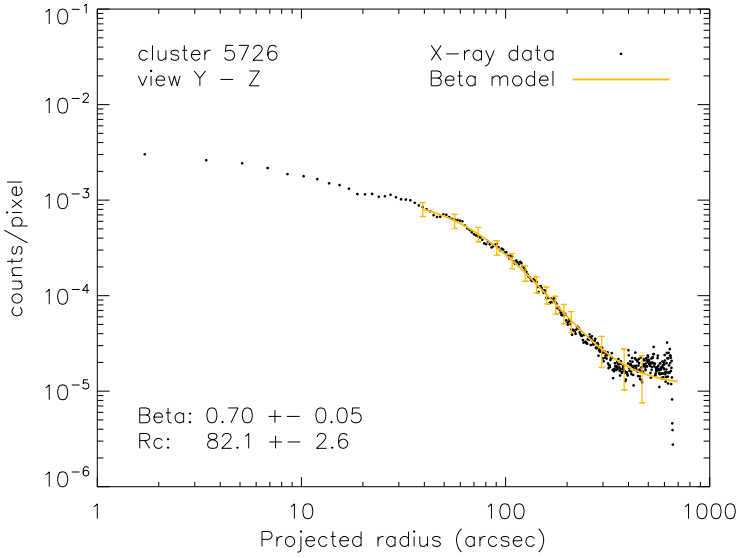

Figure 6.7: X-ray surface brightness profile of cluster 5726 and fitted β model, excluding the innermost part of the cluster. For this cluster R_{500} lies outside the field of view of XMM-Newton.

6.3 X-ray spectrum

Extraction of spectra can be performed using the XMMSAS tool `xmmselect`.

To extract the source spectrum from the observation, it is necessary to define the region to be used in the spectral extraction. For this study, the region selected is the one within radius R_{500}. The coordinates of the cluster's center obtained from the X-ray image and the R_{500} are the input to define the spectrum region.

For three out of the four clusters, the radius R_{500} is within the field of view of XMM-Newton for the given redshift. That is not the case for the most massive cluster, 5726. Figure 6.9 shows the entire field of view of XMM-Newton and the region within radius R_{500} for the clusters 5726 and 00010. There is a clear difference in the size and brightness of the two clusters.

Response files

For the spectral analysis, the response files are needed. These are the redistribution matrix file (RMF) and the ancillary response file (ARF).

The RMF matrix is generated by the XMMSAS task `rmfgen`. It describes the response of the instrument as a function of energy and pulse invariant (PI) channel. The ARF is generated by the XMMSAS task `rmfgen`. It contains a table listing area values for a number of different energy ranges.

The RMF and ARF are used to convert the observed energy distribution of photons into a incident flux distribution over energy. They can be used in conjunction to allow fitting of spectral models to the observed spectral data.

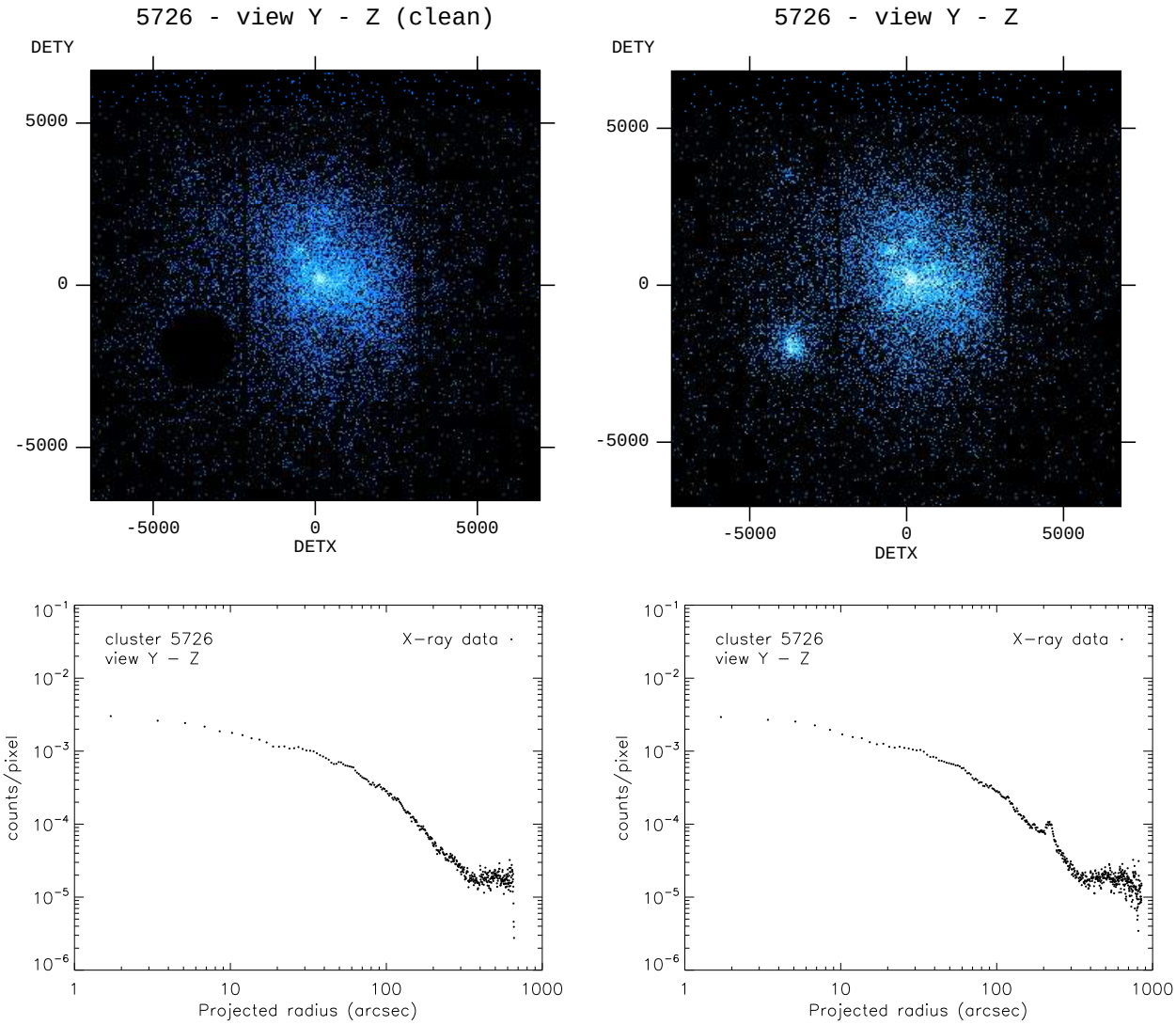

Figure 6.8: X-ray image and X-ray surface brightness profile of cluster 5726. Here we see the same image and profile before (right) and after source removal (left).

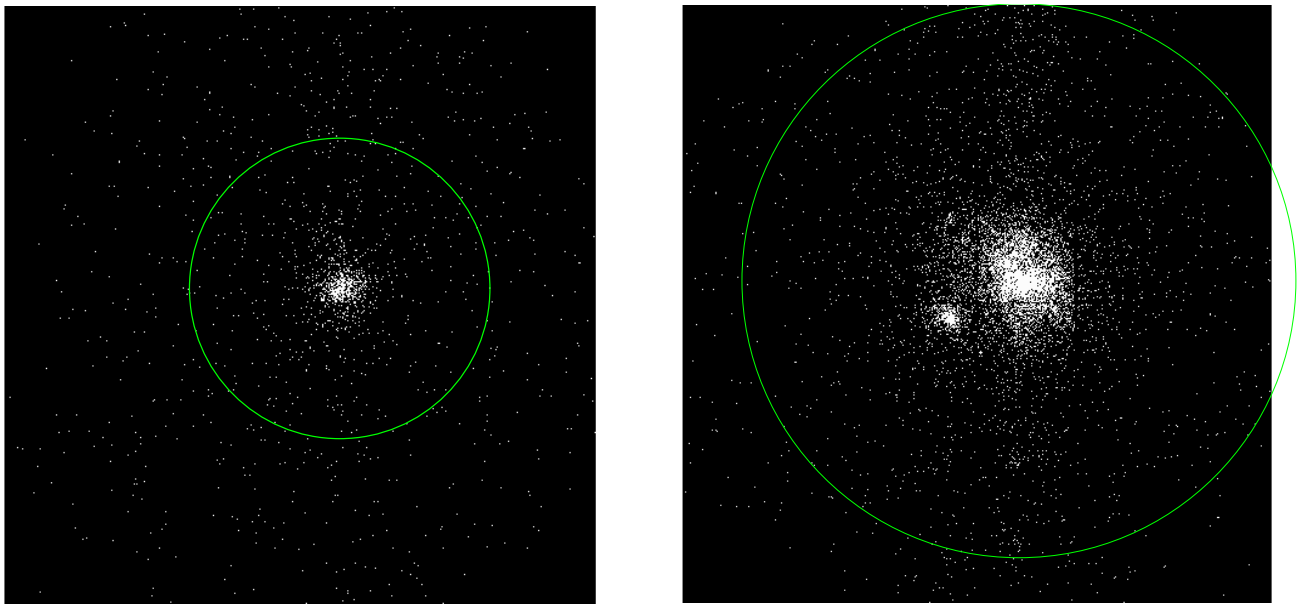

Figure 6.9: The XMM-Newton field of view and the region within R_{500} for the most massive cluster, 5726 (right), and for cluster 00010 (left).

Grouping the spectrum

The extracted spectrum is accumulated in bins containing a certain number of counts. The task `grppha`, which is part of the FTOOLS software package, is the one used for grouping the spectrum in bins.

The number of counts per bin was set to 50. For use of χ^2 statistics for spectral fitting, the number of counts per bin should be at least 20. The χ^2 statistics assumes that all the spectral channels are gaussianly distributed and that the estimate for the variance is uncorrelated with the observed counts. If there are small numbers of counts in a channel this will not be true [58].

With the grouped source spectrum, and the associated response files, we can now proceed to the spectral fitting.

6.3.1 Fitting a model to the observed spectrum

Xspec is a X-ray spectral fitting program that can be used for any detector, it has been used to analyze data from many telescopes and also for simulations [58].

Xspec reads the source spectra grouped in bins. Before Xspec can take a given set of parameter values and predict the spectrum that would be detected by a given instrument, it must know the specific characteristics of the instrument. That is provided by the response files, RMF and ARF.

The goal now is to find a model spectrum, described by few parameters, and fit it to the observed spectrum. The model parameters are varied to produce the best fit model to

the observed data. The model spectrum is calculated using the energy ranges defined by the response file [58]. The quality of the fit is measured by χ^2 statistics.

Here, we assume that the clusters are isotropic and we fit a single temperature model to the observations.

The model spectrum to fit the observed spectrum is calculated by combining the models Wabs and MeKal, `wabs(mekal)`. Details about the Wabs model and MeKal model can be found in ref. [58].

The Wabs model is a photo-electric absorption model using Wisconsin cross-sections[58]. The Wabs model accounts for the galactic absorption. The MeKal model is based on the calculations of Mewe and Kaastra for an emission spectrum from hot diffuse gas with Fe calculations by Liedahl. It includes line emissions from several elements[58].

The model parameters are the equivalent hydrogen column, plasma temperature, hydrogen density, metal abundance, redshift and a normalization parameter K.

With the exception of the redshift, which is known to be 0.1, all parameters were kept free.

Gas density

The normalization parameter K is based on the angular size distance, redshift and electron and hydrogen densities. It is defined as,

$$K = \frac{10^{-14}}{4\pi(d_A(z+1))^2} \int n_e n_H dV \quad , \tag{6.1}$$

where d_A is the angular diameter distance of the cluster, n_e and n_H are the number densities of electron and hydrogen in cm^{-3}, and the integral is over the volume of the cluster.

The angular diameter distance d_A carries the information about the cosmology assumed and it is obtained from the simulations.

Converting the number densities to mass densities, $\rho = \mu\ m_p\ n_e = \mu\ m_p\ n_H$, the normalization parameter K can be written as,

$$K = \frac{10^{-14}}{4\pi(d_A(z+1))^2} \int \left(\frac{\rho}{\mu m_p}\right)^2 dV \quad . \tag{6.2}$$

Combining Equation 6.2 and the density profile given by Equation 3.5, we have,

$$K = \frac{10^{-14}}{(d_A(z+1))^2} \left(\frac{\rho_0}{\mu m_p}\right)^2 \int_0^{R_{cl}} r^2 \left(1 + \left(\frac{r}{R_c}\right)^2\right)^{-3\beta} dr \quad , \tag{6.3}$$

where the integral now is over the cluster's radius R_{cl}.

The normalization parameter K provides information about the gas density. Knowing the value of K and the values of the parameters inside the integral in Equation 6.3, it is possible to derive the value of ρ_0, which will be used to calculate the mass of the gas.

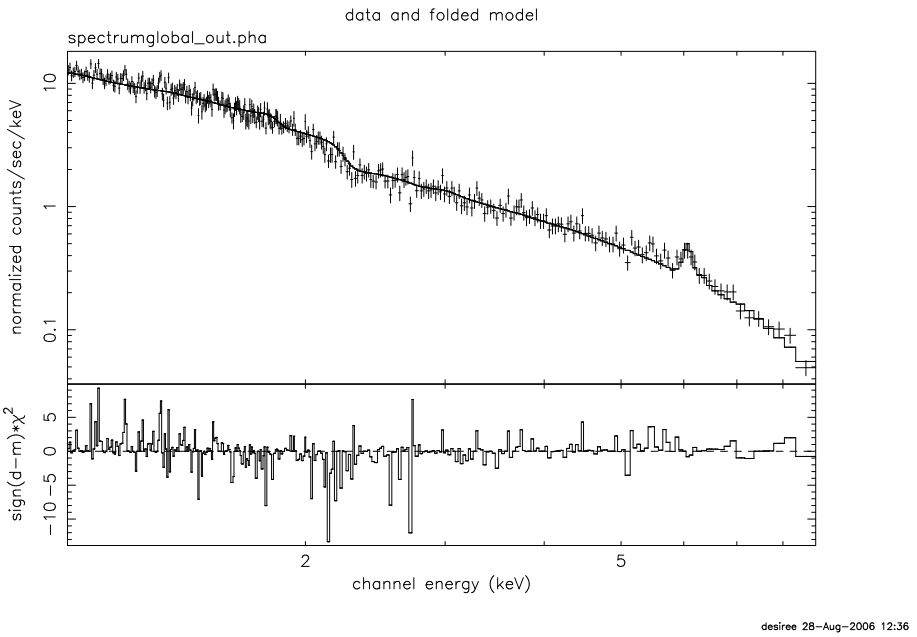

Figure 6.10: Example of X-ray spectrum and fitted model produced using Xspec.

When the fit is done, Xspec writes the best-fit parameter values, along with the 1σ confidence intervals, which are calculated from the derivatives of the fit statistic with respect to the model parameters.

The results obtained from the spectral fitting are presented in Chapter 7.

Chapter 7

Intra-cluster Medium Temperature

The temperature of the intra-cluster medium (ICM) is one of the most important characteristics of the cluster. This Chapter presents the results obtained from fitting an isothermal model to the observed X-ray spectrum in order to obtain the ICM average temperature. Here the values obtained directly for the simulations are compared to the obtained from the spectral analysis.

7.1 The average spectroscopic temperature

To derive the average temperature of the ICM it is necessary to define this quantity. The ICM average spectroscopic temperature, T_{spec}, is obtained by fitting a model to the observed spectrum. It is defined here as the best fit temperature.

For each data set an isothermal fit to the X-ray spectra was performed.

As described in Chapter 6, the model used to fit the observed spectrum is a combination of a photo-electric absorption model (wabs) and a model for an emission spectrum from hot diffuse gas accounting for line emission from several elements (MeKal) [58].

The single temperature model is fitted considering a region within R_{500}, which as mentioned previously, is the cluster radius enclosing an overdensity of 500 times the critical density. The response files are generated for the same region. The background is neglected.

The ICM is not isothermal. The X-ray emission we observe from the cluster is collapsed onto the two dimensional sky plane along the line of sight. We observe the emission of a superposition of shells of different temperatures. This makes the fitting of a single temperature model a difficult task.

Knowing that several components contribute to the observed spectrum, e.g. structures, shocks, different temperature phases, we tried to make the fit to different energy ranges to examine whether it is possible to achieve better results by ignoring the low energy part of the spectrum.

We do that by defining an energy cut, which will then work as a lower energy limit in the spectral fit. For example, if we cut the spectrum at 1 keV, that means that we are fitting a model to the X-ray spectrum considering the range between 1.0 keV and 10 keV,

ignoring all the counts with energy bellow 1.0 keV.

The results obtained for the different energy cuts for each cluster in the three orthogonal views are presented in Table 7.1.

We want to check if there is a relation between the cluster mass and the energy range considered. For that we compare the average spectroscopic temperature, T_{spec}, to the average temperature obtained directly from the simulation.

Each cluster was observed from three different views. It is expected to find similar results for the temperature since the X-ray emitting gas is the same.

Here we observe a mismatch between the results from different views. The lack of symmetry and thermal homogeneity are responsible for the discrepancies observed, together with the presence of structures that may contribute more or less to the X-ray emissivity of the gas.

Later on in this Chapter, we use temperature maps extracted from the simulation to understand the level of thermal inhomogeneity in each cluster and try to explain the mismatch between the three orthogonal observations.

7.2 Temperature from the simulations

Our goal now is to compare the ICM average temperature T_{spec} to the average temperature obtained from the simulations.

To find the ICM temperature from the simulations, we define the weighted temperature T_w,

$$T_w = \frac{\int \Lambda\left(T\right) \rho^2 T dV}{\int \Lambda\left(T\right) \rho^2 dV} \quad . \tag{7.1}$$

Here ρ is the gas density, T is the temperature, $\Lambda(T)$ is a cooling function and the integral is over the volume of the cluster. Unless stated otherwise, we define the volume of the cluster as the volume within the radius R_{500}.

For X-ray emission-weighted temperature, T_{ew}, the cooling function is defined as $\Lambda(T) \propto \sqrt{T}$, so that Equation 7.1 for emission-weighted temperature is given by,

$$T_{ew} = \frac{\int \sqrt{T} \rho^2 T dV}{\int \sqrt{T} \rho^2 dV} \quad . \tag{7.2}$$

The T_{ew} is not an observable quantity but can be used to compare T_{spec} obtained from fitting a model to the X-ray spectra to the real ICM temperature. It has been conventionally assumed that T_{spec} is approximately equal to T_{ew} [59].

It's been recognized that there is a mismatch between T_{spec} and T_{ew} [60, 61]. To solve this problem, an alternative definition for the average T_{spec} has been proposed. This is called the spectroscopic-like temperature, T_{sl}.

For the spectroscopic-like temperature T_{sl}, the cooling function has been calibrated by [60] and it is $\Lambda(T) \propto 1/T^{\alpha}$, with $\alpha = 0.75$.

Cluster	Cut (keV)	T_{spec}^{y-z} (keV)	T_{spec}^{x-z} (keV)	T_{spec}^{x-y} (keV)
5726	0.5	4.79 ± 0.11	4.64 ± 0.07	4.88 ± 0.11
	1.0	5.61 ± 0.12	5.30 ± 0.13	5.66 ± 0.17
	1.5	6.34 ± 0.33	5.23 ± 0.16	5.99 ± 0.28
	2.0	5.74 ± 0.36	4.40 ± 0.17	5.67 ± 0.31
	2.5	5.51 ± 0.43	3.81 ± 0.14	4.70 ± 0.29
	3.0	5.05 ± 0.47	3.38 ± 0.17	4.13 ± 0.29
00010	0.5	3.47 ± 0.07	2.95 ± 0.09	3.24 ± 0.08
	1.0	3.65 ± 0.09	3.42 ± 0.18	3.73 ± 0.10
	1.5	4.10 ± 0.14	3.48 ± 0.27	4.11 ± 0.24
	2.0	4.37 ± 0.20	3.71 ± 0.42	4.46 ± 0.38
	2.5	4.22 ± 0.24	3.20 ± 0.42	3.72 ± 0.32
	3.0	3.82 ± 0.23	3.21 ± 0.56	3.99 ± 0.46
25174	0.5	1.97 ± 0.05	2.66 ± 0.06	2.84 ± 0.06
	1.0	2.23 ± 0.09	3.04 ± 0.11	3.22 ± 0.07
	1.5	2.23 ± 0.07	3.30 ± 0.18	3.64 ± 0.11
	2.0	2.51 ± 0.18	3.53 ± 0.16	3.72 ± 0.25
	2.5	2.67 ± 0.31	3.71 ± 0.39	3.50 ± 0.36
	3.0	2.44 ± 0.26	3.73 ± 0.41	3.67 ± 0.57
21926	0.5	3.26 ± 0.11	3.13 ± 0.11	2.27 ± 0.10
	1.0	3.76 ± 0.22	3.45 ± 0.19	2.76 ± 0.22
	1.5	4.15 ± 0.35	3.89 ± 0.32	3.36 ± 0.51
	2.0	4.82 ± 0.58	3.43 ± 0.38	4.57 ± 1.70
	2.5	3.96 ± 0.51	3.61 ± 0.59	3.64 ± 1.70
	3.0	4.15 ± 0.77	3.80 ± 0.65	5.03 ± 5.04

Table 7.1: Average temperature T_{spec} obtained from fitting a model to the observed X-ray spectrum considering different energy ranges. The scatter observed in the values obtained for different views indicates the thermal inhomogeneity of the ICM.

Cluster	M_{500} ($M_\odot$)	T_{ew} (keV)	T_{sl} (keV)
5726	9.91 $\times 10^{14}$	7.25 $\pm$ 1.40	4.70 $\pm$ 1.80
00010	1.92 $\times 10^{14}$	3.55 $\pm$ 0.52	3.18 $\pm$ 0.77
24174	1.90 $\times 10^{14}$	2.78 $\pm$ 0.28	2.62 $\pm$ 0.32
21926	1.31 $\times 10^{14}$	2.51 $\pm$ 0.32	2.23 $\pm$ 0.56

Table 7.2: This table presents the X-ray emission-weighted temperature, T_{ew}, and spectroscopic-like temperature, T_{sl}, obtained from the simulations. Here we observe that the temperature increases with the cluster mass. We also notice that T_{sl} is systematically lower than T_{ew}. The most massive cluster presents the larger mismatch between the temperatures indicating high thermal inhomogeneity.

The Equation 7.1 for the spectroscopic-like temperature takes the form,

$$T_{sl} = \frac{\int \rho^2 T^\alpha T^{-1/2} dV}{\int \rho^2 T^\alpha T^{-3/2} dV} \quad . \tag{7.3}$$

For each cluster in our sample we calculate both T_{ew} and T_{sl}, within R_{500}. The results are shown in Table 7.2.

7.3 Comparing results

Comparing the temperature values obtained to the mass of the clusters we observe that larger clusters have higher temperatures. In Chapter 9 it is discussed how the mass scales with the temperature.

We observe also that the spectroscopic-like temperature, T_{sl} is systematically lower than the emission-weighted temperature, T_{ew}. However, for three out of the four clusters the results agree within the error bars.

Confronting T_{ew} and T_{sl} to the observation values, T_{spec}, we observe that for three out of four clusters there is no significant difference between how well they approximate T_{spec}. For the most massive cluster, 5726, this picture changes.

For cluster 5726, T_{ew} overestimates T_{spec}, while T_{sl} reproduces T_{spec} much better.

Previous studies by [60] showed that if the cluster is highly thermally inhomogeneous then the average temperature obtained from spectral fitting, T_{spec}, is significantly lower than the average emission-weighted temperature, T_{ew}. In this way, T_{ew} overestimates T_{spec} obtained from X-ray observations. The agreement between the two temperatures depends on the complexity of the cluster thermal structure [62].

This result confirms the high thermal inhomogeneity of the most massive cluster. It should be pointed out that the X-ray image analysis already indicates that this cluster is not the best example of relaxed cluster, presenting lack of symmetry and structures.

For the least massive cluster, 21926, both T_{ew} and T_{sl} underestimate T_{spec}. Here the high temperature values obtained from the observations of this cluster could be a result

of a poor spectral fit. When performing the virtual observations of the simulated clusters, the same exposure time for all clusters was adopted, independent of their masses.

The observation of cluster 21926 contains a lower number of counts. When these are then grouped in bins to fit the observed spectrum we do not have the same quality as we do for the more massive clusters. The spectral fit is generally poor and the energy cuts adopted are only increasing the errors.

The solution to this problem is to perform the virtual observation of this cluster with a longer exposure time in order to get a data set of better quality.

In Figure 7.2, T_{ew} is compared to T_{spec} for each cluster and the three orthogonal views. The solid line represents T_{ew}, and the dashed line its error. We plot T_{spec} obtained from considering different energy ranges when fitting a model to the spectrum.

Figure 7.3 presents the same results, now comparing with the spectroscopic-like temperature, T_{sl}.

Looking at the results of T_{spec} obtained for different energy ranges we observe that the two least massive clusters, 25174 and 21926, reproduce better both T_{ew} and T_{sl} if we consider the energy cut at 0.5 keV. For cluster 00010, the energy cut at 1.0 keV seems to be the best choice. For the most massive cluster, 5726, an energy cut at 1.5 keV approximates best T_{ew}.

Here the energy range appears to be dependent on the mass with a mild trend that higher cluster mass would require a higher energy cut. However, no definitive picture emerges from this first analysis. A larger sample of clusters is necessary to determine this dependence.

7.4 Temperature maps

Temperate maps were extracted from the simulations. Here an IDL procedure is used to smooth the temperature of the gas according to the line of sight defined by the viewing angle.

These maps were produced considering the XMM-Newton field of view and the same three orthogonal views used to observe the clusters in our sample.

The temperature maps are used to identify the thermal condition of the clusters and to try to understand how this relates to the average temperature obtained from the spectral fitting.

The temperature maps of the most massive cluster, 5726, are shown in Figure 7.4. They reveal a highly inhomogeneous thermal condition. This explains the mismatch between the emission-weighted temperature and spectroscopic-like temperature. It agrees with the results obtained by [62] where the agreement between the two temperatures depends on the thermal complexity of the cluster.

For cluster 00010, the temperature map presents a more relaxed gas. From the maps we would expect the average temperature from the X-ray observation to be higher for view Y-Z, and lower for view X-Z because of the presence of a cool bubble close to the center. This is actually reproduced in the values of T_{spec} we obtain.

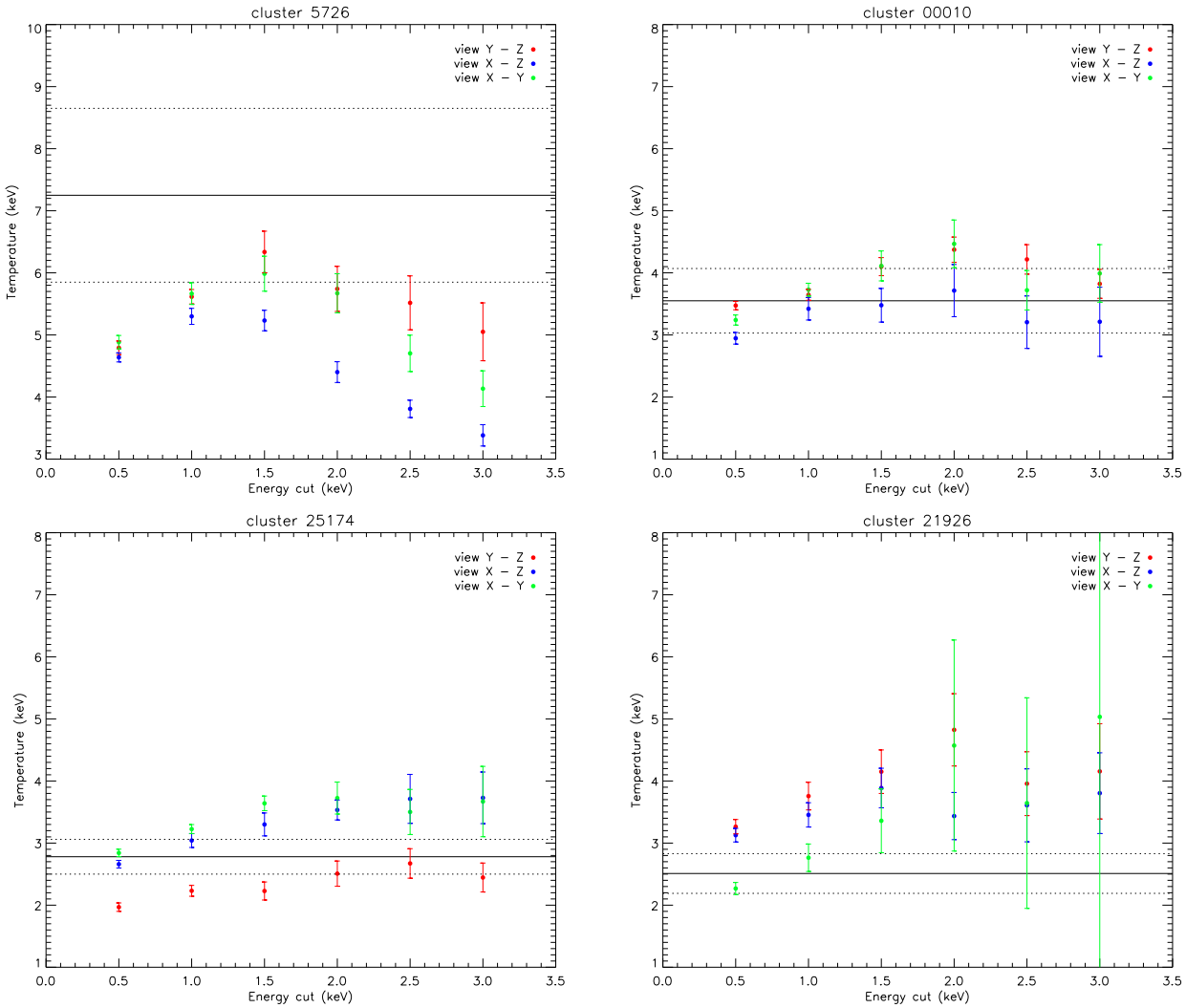

Figure 7.1: The plots show the average spectroscopic temperature, T_{spec}, obtained from the observations, considering different energy ranges in fitting a model to the X-ray spectrum. The solid line represents the emission-weighted temperature, T_{ew}. The dashed line represents the T_{ew} error. Here we see the mismatch between the temperatures obtained from different views.

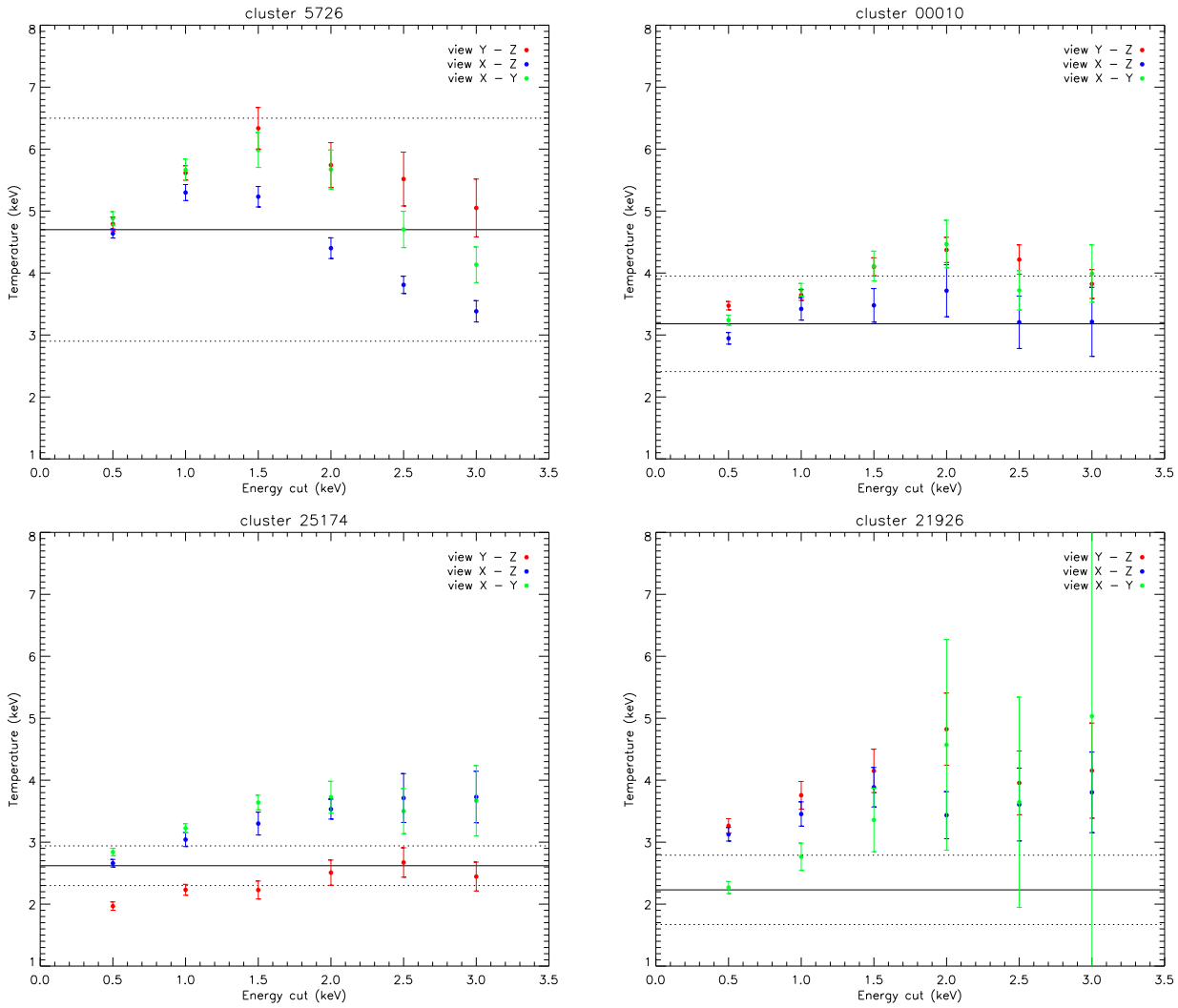

Figure 7.2: Plots of the average spectroscopic temperature, T_{spec}, obtained from the observations, considering different energy ranges in fitting a model to the X-ray spectrum. The solid line represents the spectroscopic-like temperature, T_{sl}. The dashed line represents the T_{sl} error. For cluster 5726 T_{sl} reproduces T_{spec} better than T_{ew}.

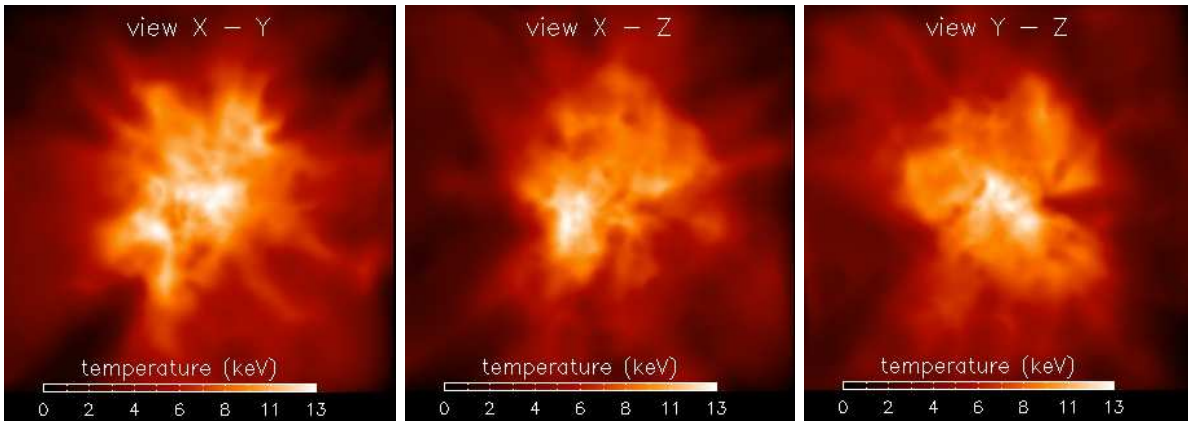

Figure 7.3: Temperature maps of cluster 5726 within the field of view of XMM-Newton. This is the most massive cluster in our sample.It appears to be highly thermally inhomogeneous. A hot cluster core is not well defined showing cooler regions and lack of symmetry.

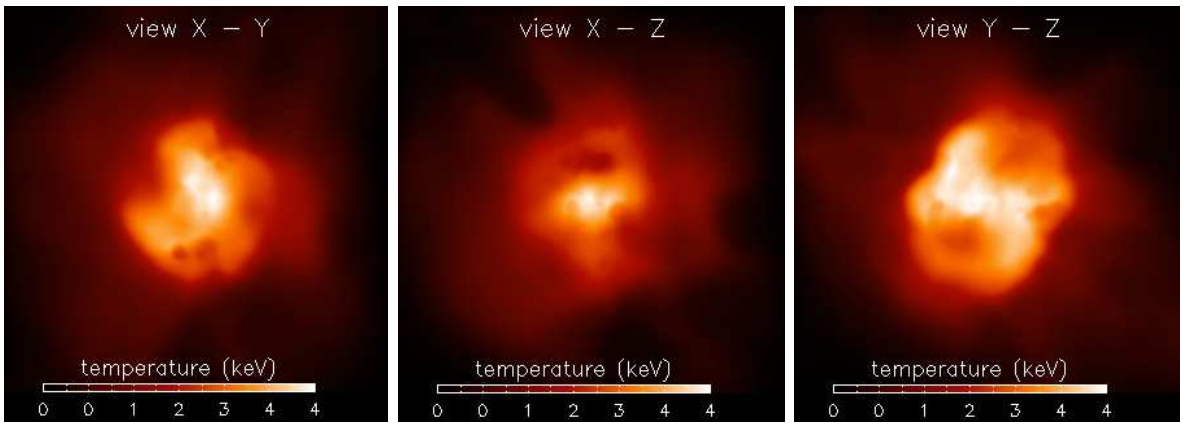

Figure 7.4: Temperature maps of cluster 00010 within the field of view of XMM-Newton. For this cluster T_{spec} reproduces the situation observed in the temperature map, with a lower value for T_{spec}^{x-z}, probably due to the presence of a cooler region near the cluster center.

Cluster 25174 presents a lower value of T_{spec} for the view Y-Z. The temperature map of this view shows that the warm region appears to be slightly smaller then in the other two views. This lack of symmetry could be the responsible for the lower average temperature obtained for view Y-Z.

The temperature maps of cluster 21926 do not present significant difference between the three views. In the X-Y view, the hot region is slightly smaller than in the other views. Here again, this would account for the lower value of T_{spec} obtained for this view.

7.5 Temperature profile

The temperature profiles for each cluster were obtained dividing the cluster spectrum into annuli and fitting an isothermal model to each annulus. The annuli were generated

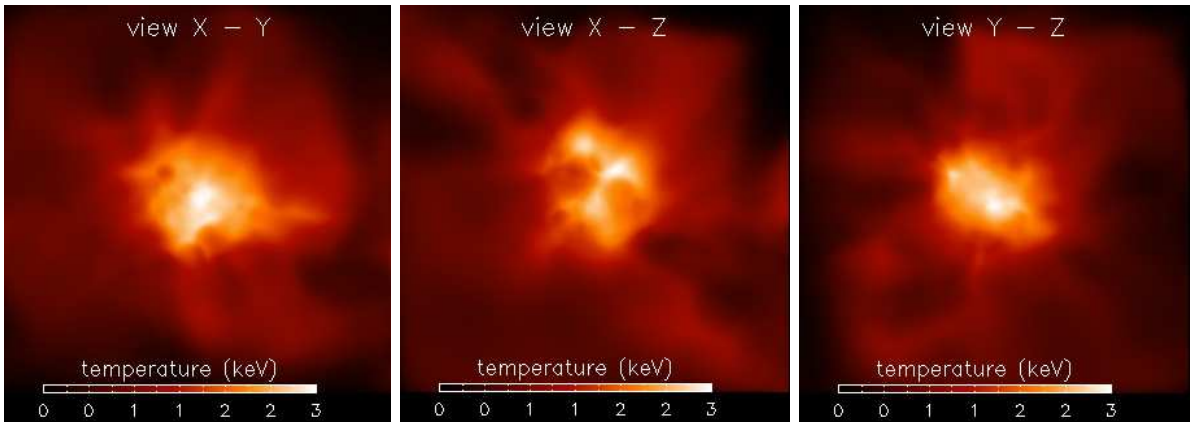

Figure 7.5: Temperature maps of cluster 25174 within the field of view of XMM-Newton.

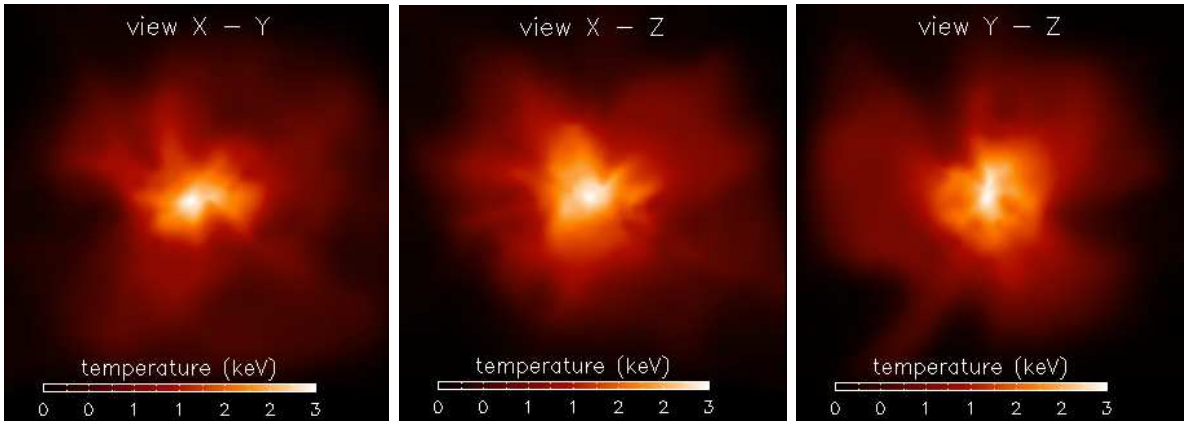

Figure 7.6: Temperature maps of cluster 21926 within the field of view of XMM-Newton.

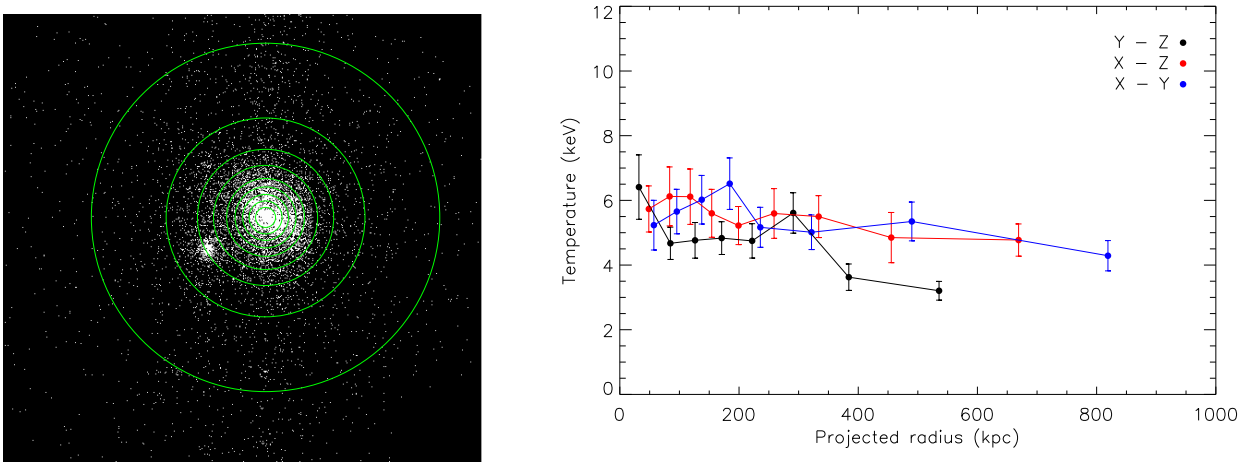

Figure 7.7: X-ray image with the annuli considered for computing the temperature profile of cluster 5726, view X-Y (left), and the temperature profiles derived for each view (right).

containing 5000 counts each, starting from the cluster center. The response matrices were also generated for each annulus.

The only relevant profile considering this amount of counts is the one obtained for the most massive cluster, 5726. Because the number of counts obtained for the other clusters is significantly smaller than for the most massive cluster, we ended up with two or three annuli, which do not provide good enough data for extracting relevant information from the profile.

Future work includes the observation of these clusters with higher exposure time in order to get enough precision to produce good quality temperature profiles.

The profile obtained for the most massive cluster is presented here. Figure 7.5 shows the X-ray image with the annuli considered and the profile derived from fitting an isothermal model to each spectrum extracted, considering an annulus region.

The temperature profiles are relevant in deriving the cluster mass and mass profiles [63]. In this study we considered an isothermal ICM, not including the temperature gradients when calculating the total mass of the clusters using Equation 3.3.

At least for cluster 5726, which presents high thermal inhomogeneity, it is expected that neglecting the temperature gradients will reflect significantly in the value of the total cluster mass.

7.6 Discussion

For our cluster sample, the ICM average spectroscopic temperatures, T_{spec}, were obtained by fitting an isothermal model to the X-ray spectra observed in three orthogonal views.

For a perfectly relaxed cluster, the results from different views would be expected to be the same, since we are studying the X-ray emission of the same gas. However, the

observations lead us to different results. We observe a mismatch between T_{spec} in different observation angles. This happens because of lack of symmetry and the thermal inhomogeneity of the clusters. This scenario is supported by the temperature maps extracted from the simulations, revealing the thermal condition of the clusters.

The X-ray emission-weighted temperatures, T_{ew}, and the spectroscopic-like temperatures, T_{sl}, we obtained directly from the simulations. We observe that for the most massive cluster T_{ew} overestimates T_{spec}, while T_{sl} approximates T_{spec} better. The difference between T_{ew} and T_{sl} depends on the thermal complexity of the cluster and increases with complexity. This indicates that the most massive cluster presents high thermal inhomogeneity. For the three other clusters in our sample T_{ew} and T_{sl} agree within the error bars.

When fitting a model to the X-ray spectra, different energy ranges were considered in order to test for systematics relating the energy range considered to the cluster mass. A mild trend that more massive clusters would require higher energy cuts is observed but we need a larger cluster sample to determine this dependence.

Here it is observed from the temperature maps and temperature profiles that the ICM is not isothermal. Including the temperature profile in the analysis will provide a more realistic description of the thermal condition of the clusters, providing information about the physics going on in the ICM.

Chapter 8

Cluster Mass

This chapter presents the computed cluster masses obtained by combining the results from the spectral and the image analysis. Here the results from the observations are compared to the values obtained from the simulations.

8.1 Total mass

By comparing the results from our virtual observation to the data from the simulations, the applicability and accuracy of the assumption of hydrostatic equilibrium to derive the cluster mass can be tested.

Assuming spherical symmetry and hydrostatic equilibrium of the X-ray emitting gas, the total cluster mass inside a radius R can then be calculated.

The masses of X-ray emitting gas and the total cluster mass for each cluster were calculated considering the cluster outer radius R_{500}, which is the radius containing a cluster mean density equal to 500 times the critical density of the Universe. Equation 3.3 takes the form,

$$M_{500} = -\frac{kTR_{500}}{G\mu m_p}\left(\frac{d\ \ln\ \rho_{gas}}{d\ \ln\ r} + \frac{d\ \ln\ T}{d\ \ln\ r}\right) \quad . \tag{8.1}$$

Here M_{500} is the total cluster mass within radius R_{500} and r is the projected radius. In real observations it is not possible to know the precise value of R_{500}, it has to be inferred from models of the density profile and cluster scaling relations such as luminosity and temperature [38, 64].

Here the gas is considered as a fully ionized plasma, with mean molecular weight $\mu = 0.6$. It is assumed that the intra-cluster medium is isothermal. Under this assumption, the temperature profiles were not considered, and Equation 8.1 becomes,

$$M_{500} = -\frac{kTR_{500}}{G\mu m_p}\left(\frac{d\ \ln\ \rho_{gas}}{d\ \ln\ r}\right) \quad . \tag{8.2}$$

The density profile of the gas, $(d \ln \rho_{gas} / \ln r)$, is estimated by fitting a β model to the X-ray surface brightness profile,

$$S(r) \propto \left(1 + \left(\frac{r}{R_c}\right)^2\right)^{-3\beta+\frac{1}{2}} \quad . \tag{8.3}$$

From the best-fit parameters, β and the core radius R_c are obtained. These values are used to determine the density profile,

$$\rho_{gas}(r) \propto \left(1 + \left(\frac{r}{R_c}\right)^2\right)^{-\frac{3}{2}\beta} \quad . \tag{8.4}$$

To compute the cluster total mass a temperature is needed. For that the average temperature obtained from the spectral fitting is used. The masses were calculated considering the temperatures obtained by fitting the X-ray spectrum considering different energy ranges. Figure 8.1 presents the results for each cluster. Here the results obtained for the three orthogonal views are presented and can be compared to the real cluster mass obtained from the simulations.

The results obtained for different views of the clusters are not the same since the parameters derived from the X-ray spectral analysis and X-ray brightness profiles for different views also differ.

Table 8.1 presents the best results obtained for the clusters total masses.

For the most massive cluster, 5726, the computed masses are much lower than the mass obtained directly from the simulations. This mismatch is due to the presence of structures, lack of symmetry and thermal inhomogeneity. The observed temperature, T_{spec} is significantly lower than the emission weighted temperature obtained from the simulations for this cluster, which results in a lower total mass, since the mass is proportional to the temperature. The temperature maps of cluster 5726 extracted from the simulations show a highly thermally inhomogeneous ICM. The assumption of isothermality is not satisfying for this cluster and indicates that the cluster total mass is dependent on the temperature profile.

For cluster 00010, the results obtained are the ones that best reproduce the real cluster mass. The mismatch between the values obtained for different views is smaller than the ones obtained for the other clusters. This cluster appears to be spherically symmetric and does not present structures like cluster 5726 does. To consider the temperature profiles may improve the results making the assumption of hydrostatic equilibrium robust for this system.

Clusters 25174 and 21926 present both good mass estimations for two out of three views. This is directly connected to the temperature value obtained from the spectral analysis. For both clusters the larger errors in the masses are basically the propagation of the temperature error since from Equation 8.2, considered for the calculation, the mass is

Cluster	M_{sim} ($10^{14} M_{\odot}$)	View	β	T_{spec} (keV)	$M_{500}(10^{14} M_{\odot})$	$Error_{mass}$
5726	9.91	y - z	0.70 ± 0.05	6.34 ± 0.33	7.41 ± 0.70	25%
		x - z	0.64 ± 0.03	5.23 ± 0.16	5.59 ± 0.33	43%
		x - y	0.65 ± 0.04	5.99 ± 0.28	6.54 ± 0.54	34%
00010	1.92	y - z	0.65 ± 0.01	3.47 ± 0.07	2.14 ± 0.09	11%
		x - z	0.74 ± 0.05	2.95 ± 0.09	1.96 ± 0.19	2%
		x - y	0.66 ± 0.02	3.24 ± 0.08	1.93 ± 0.10	0.5%
24174	1.90	y - z	0.63 ± 0.01	2.23 ± 0.09	1.36 ± 0.06	28%
		x - z	0.63 ± 0.01	3.04 ± 0.11	1.87 ± 0.08	2%
		x - y	0.59 ± 0.01	3.22 ± 0.07	1.85 ± 0.06	3%
21926	1.31	y - z	0.58 ± 0.02	3.26 ± 0.11	1.62 ± 0.12	23%
		x - z	0.49 ± 0.02	3.13 ± 0.11	1.33 ± 0.09	1.5%
		x - y	0.53 ± 0.03	2.27 ± 0.10	1.02 ± 0.09	22%

Table 8.1: The table presents the best results for the clusters total masses. Here it was considered an energy cut of 1.5 keV for the most massive cluster, 0.5 keV for clusters 00010 and 21926 and 1.0 keV for cluster 24174. The best mass estimation is for cluster 00010.

proportional to the temperature. To consider temperature profiles may improve the results but here the lack of symmetry due to thermal inhomogeneity of the gas seems to be the main reason for the mismatch observed.

Another source of error for the mass values comes from the fitting of a single β model to the X-ray surface brightness profile. Alternative methods, e.g. using a double β model to fit the observed profile, may improve the results.

Concerning the energy ranges in the spectral fit, even though it seems that the most massive cluster would require a higher energy cut to reproduce better the real cluster mass, no definitive picture relating the energy cuts to the clusters masses can be defined from our sample. In this way a universal cut value at 1.0 keV was considered for the further analysis.

8.2 Gas mass and gas mass fraction

To determine the mass of the hot X-ray emitting gas, the density profile given by Equation 3.5 is integrated over the volume of the cluster within radius R_{500},

$$M_{gas} = \int \rho_{gas} \ dV \ . \tag{8.5}$$

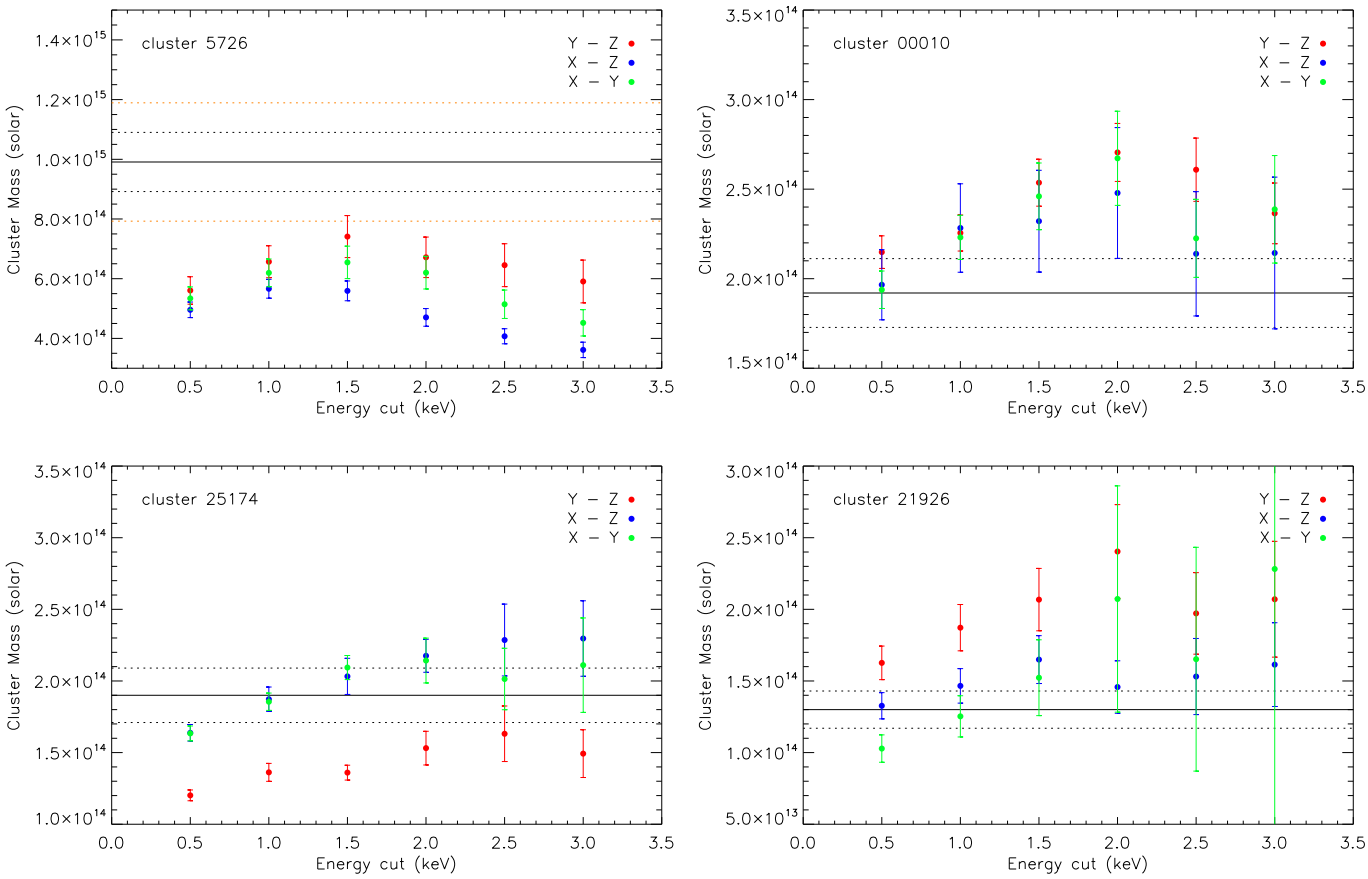

Figure 8.1: Total cluster masses considering different energy cuts for the X-ray spectral fit. The solid line represents the real cluster mass obtained directly from the simulations. The dashed lines represent the masses within 10% error. For cluster 5726, the colored dashed line represents the mass within 20% error.

Cluster	T_{ew} (keV)	M_{sim} ($10^{14} M_{\odot}$)	view	T_{spec} (keV)	$M_{500}(10^{14} M_{\odot})$	$Error_{mass}$
5726	7.25 ± 1.40	9.91	y - z	5.61 ± 0.12	6.57 ± 0.53	34%
			x - z	5.30 ± 0.13	5.66 ± 0.31	43%
			x - y	5.66 ± 0.17	6.19 ± 0.46	37%
00010	3.55 ± 0.52	1.92	y - z	3.65 ± 0.09	2.25 ± 0.10	17%
			x - z	3.42 ± 0.18	2.28 ± 0.25	19%
			x - y	3.73 ± 0.10	2.23 ± 0.12	16%
24174	2.78 ± 0.28	1.90	y - z	2.23 ± 0.09	1.36 ± 0.06	28%
			x - z	3.04 ± 0.11	1.87 ± 0.08	2%
			x - y	3.22 ± 0.07	1.85 ± 0.06	3%
21926	2.51 ± 0.32	1.31	y - z	3.76 ± 0.22	1.87 ± 0.16	43%
			x - z	3.45 ± 0.19	1.46 ± 0.12	11%
			x - y	2.76 ± 0.22	1.25 ± 0.14	4%

Table 8.2: The table presents the emission weighted temperatures, T_{ew}, and the clusters total masses, M_{sim}, obtained from the simulations, the average temperatures, T_{spec}, obtained by fitting a model to the X-ray spectra considering the energy cut at 1 keV, the computed clusters total masses within R_{500}, together with the error between simulation and observation, $Error_{mass}$.

With the density profile given by,

$$\rho_{gas}(r) = \rho_0 \left(1 + \left(\frac{r}{R_c}\right)^2\right)^{-\frac{3}{2}\beta} \quad , \tag{8.6}$$

we have the gas mass within R_{500},

$$M_{gas} = 4\pi\rho_0 \int_0^{R_{500}} r^2 \left(1 + \left(\frac{r}{R_c}\right)^2\right)^{-\frac{3}{2}\beta} dr \quad . \tag{8.7}$$

The values of β and R_c are obtained from fitting a β model to the X-ray surface brightness profile, while ρ_0 is computed from the normalization parameter obtained by fitting a model to the X-ray spectrum, as described in Chapter 6.

The gas mass computed for each data is presented in Table 8.2.

For the most massive cluster, 5726, the results obtained for the gas mass reproduce the values extracted from the simulations better than the values of the total cluster mass. This happens because the temperature profiles are not needed when calculating the mass of the gas. To not consider the temperature profiles has an impact in the total cluster mass but it doesn't interfere with the computed values of the gas mass.

The main source of error in the determination of the gas mass comes from the normalization parameter in the spectral fit. This parameter is used to compute the gas density.

Cluster	M_{gas}^{sim} $(10^{13} M_{\odot})$	View	M_{gas}^{obs} $(10^{13} M_{\odot})$	$Error_{gas}$
5726	9.50	y - z	6.77 ± 0.68	28%
		x - z	8.08 ± 0.52	15%
		x - y	7.58 ± 0.58	20%
00010	1.74	y - z	1.58 ± 0.11	9%
		x - z	1.37 ± 0.18	21%
		x - y	1.59 ± 0.14	9%
25174	1.70	y - z	1.54 ± 0.10	9%
		x - z	1.56 ± 0.13	8%
		x - y	1.78 ± 0.10	5%
21926	1.21	y - z	1.20 ± 0.14	1%
		x - z	1.55 ± 0.11	28%
		x - y	1.15 ± 0.15	5%

Table 8.3: This table presents the values of the gas masses extracted from the simulations, M_{gas}^{sim}, and the computed values from the observations, M_{gas}^{obs}, together with the error between the two quantities, $Error_{gas}$.

Cluster	f_{gas}^{sim}	View	f_{gas}^{obs}
5726	0.09	y - z	0.10 ± 0.02
		x - z	0.14 ± 0.02
		x - y	0.12 ± 0.02
00010	0.09	y - z	0.07 ± 0.01
		x - z	0.06 ± 0.01
		x - y	0.07 ± 0.01
25174	0.09	y - z	0.11 ± 0.01
		x - z	0.08 ± 0.01
		x - y	0.09 ± 0.01
21926	0.09	y - z	0.06 ± 0.01
		x - z	0.10 ± 0.01
		x - y	0.06 ± 0.01

Table 8.4: This table presents the results of the gas mass fractions considering the clusters total masses and gas masses extracted from the simulations, f_{gas}^{sim}, and the masses computed from the X-ray analysis, f_{gas}^{obs}.

In this way, the errors obtained in the gas mass come from fitting a single temperature model to the spectrum of a thermally inhomogeneous gas.

The gas mass fractions, $f_{gas}^{obs} = M_{gas}^{obs}/M_{500}$, were calculated and are presented in Table 8.2 along with the associated errors obtained from standard error analysis.

The parameters derived from the X-ray study of the galaxy clusters used to compute the cluster total mass and the gas mass are the same. In this way it would be expected that the discrepancies in the gas mass fraction to be smaller since the same error propagated to the cluster total mass is also propagated to the gas mass. Here again the temperature profiles, that were not considered in the derivation of the cluster total mass, could improve the agreement between the gas mass fractions obtained from the simulations and the ones obtained from observations.

Chapter 9

Mass-Temperature Relation

The purpose of this Chapter is to present and discuss how the masses of the clusters used in this study scale with their observed average temperatures, comparing the results obtained to theoretical predictions and previous studies.

9.1 Power law fit

The application of clusters of galaxies to derive cosmological parameters rely on the scaling relations between the clusters observables and the total mass. The study of mass-temperature relation provide the link between the hot intra-cluster gas and the total cluster mass.

To investigate the mass-temperature relation in our cluster sample, the average spectroscopic temperatures, T_{spec}, were used. These were obtained by fitting of an isothermal model to the X-ray spectra considering the energy range 1.0 to 10.0 keV. The total masses of the clusters were computed under the assumption of hydrostatic equilibrium, spherical symmetry and isothermality of the intra-cluster medium within a radius R_{500}.

To check how the cluster mass scales with the average temperature, the mass-temperature relation obtained considering the 12 data sets was fitted with a power law of the form,

$$M_{500} = A \left[\frac{T_{spec}}{1keV}\right]^{\alpha} \quad . \tag{9.1}$$

Here A and α are the parameters that will vary to produce the best fit to the observed data. For the sample used in this study, the best-fit parameters are $\alpha = 1.74 \pm 0.04$ and $A = (2.47 \pm 0.32) \times 10^{13} M_{\odot}$.

Figure 9.1 presents the mass-temperature relation of the sample analyzed, and the fitted power law.

The scatter in the mass estimation with respect to the true cluster mass obtained from the simulations was computed for this sample and is $\sigma_{mass} = 0.36$, most of which is due to the massive cluster 5726, which presents the largest discrepancies between the observed and

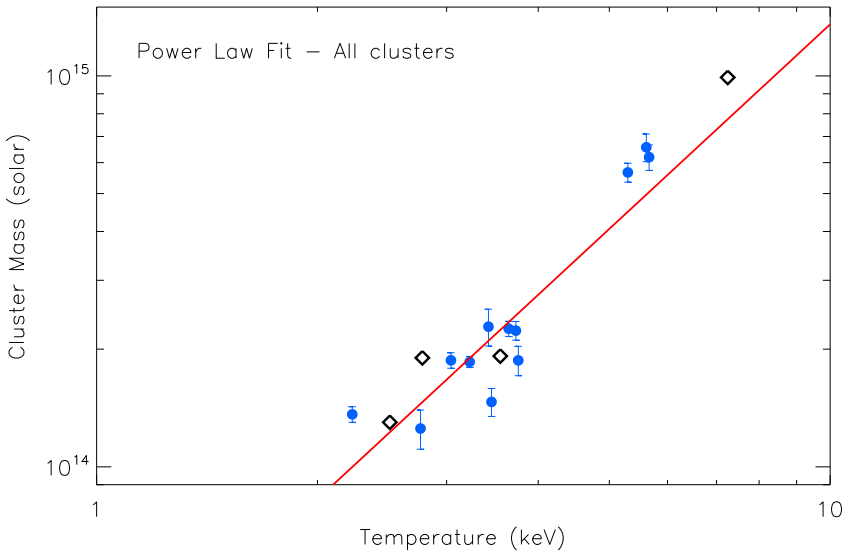

Figure 9.1: The mass-temperature relation of our cluster sample. Here the red line represents the power law fitted to the results obtained for the 12 data sets. In black it is included the real masses and their respective emission-weighted temperatures obtained from the simulations. The power law fit was performed considering only the observed masses. We obtain a slope $\alpha = 1.74 \pm 0.04$, which is steeper than the predicted by the self-similar models.

simulated masses. The scatter obtained for the mass-temperature relation is $\sigma_{m-t} = 0.22$. The scatter of the mass-temperature relation is an indicator of how well the temperature can be used as an estimator of the total mass.

The mass-temperature relation depends on the assumptions used in deriving the total masses of the clusters and how the average temperature is defined [65]. A good mass estimation is crucial for using this relation to derive cosmological parameters from galaxy clusters. The sources of errors and biases in the derivation of the total masses of and average temperatures are discussed in Chapters 7 and 8. These come come mainly from departure of hydrostatic equilibrium, non-isothermality of the intra-cluster medium and systematic errors in the derived average temperatures.

The errors in the temperatures will produce errors in the computed total masses. However, these errors should not interfere with the mass-temperature relation.

9.2 Comparing results

A tight correlation between the temperature of the intra-cluster medium and the total cluster mass is expected on theoretical grounds. Numerical calculations of structure formation based solely on gravitation make predictions on the scaling laws in galaxy clusters. It is expected that clusters of different sizes to be a scaled version of each other as long as gravity is the only process in act. For the standard self-similar model, the total cluster

mass scales with the temperature as $M \propto T^{3/2}$.

The prediction from the simulations has been tested by observational results and disagreements have been found concerning the predicted slope. In previous studies, [66] derived a slope of $\alpha = 1.51 \pm 0.27$ consistent to the self-similar prediction for a set of five hot massive clusters ($T \geq 5$ keV), [9] find a slope consistent with the self-similar model for a sub sample containing clusters with temperature $T \geq 3$ keV, [67] find a slope in agreement with the self-similar model for a sample including also low temperature systems if the gas temperatures are measured excluding the central core regions.

The slope of $\alpha = 1.74 \pm 0.04$ computed in this study is steeper than the predicted by the self-similar model, but agrees with the results obtained by [40, 39, 69], which consider a cluster sample also including low temperature systems. The derived slope also agrees with the results obtained by [9], which obtain a slope of $\alpha = 1.70 \pm 0.07$ when using the complete sample, including the low temperature clusters, for the derivation of the mass-temperature slope.

The steeper slope in the mass-temperature relation may suggest that other processes than gravitational collapse play a role in the heating of the intra-cluster medium.

As presented above, it is still unclear whether the total cluster mass scales with the temperature as predicted by the self-similar models or if this relation is true only for high temperature systems. Two out of the four clusters analyzed in this study have temperature $T_{spec} \leq 3$ keV, and here we reproduce the steeper slope observed by previous studies including low temperature clusters. A sample containing a wide range of temperatures should provide clarification of this matter.

Another remark is that the cluster samples analyzed in most of the previous studies on mass-temperature relation are made of relaxed clusters, which represent only a fraction of the total cluster population. This biases the sample. A study of larger, unbiased sample, is necessary to determine a definitive picture of the mass-temperature relation.

Chapter 10

Summary

This thesis reports the results obtained from the XMM-Newton virtual observation of simulated galaxy clusters.

Systematics that affect the cluster total mass measurements from X-ray studies and the relation between the cluster total mass and temperature were investigated by using simulated galaxy clusters observed by the simulator of the XMM-Newton Observatory, SciSim [54]. The aim was to produce realistic simulated event files that are processed and analyzed in the same way that is done with real observed clusters, to test for biases in the determination of the total masses of the clusters and in the mass-temperature relation.

A sample was selected containing four simulated galaxy clusters of different masses, extracted from a hydrodynamic simulation using the cosmological code GADGET-2. The same methods of data reduction and analysis were applied on the four galaxy clusters.

A pipeline that enabled us to read the data from the simulation and prepare it to be observed by SciSim was used. Each cluster was observed from three orthogonal views in order to test for inhomogeneities and lack of spherical symmetry. That makes up 12 data sets that were reduced and analyzed independently.

For all procedures in the data reduction and analysis the clusters radius at R_{500} was considered. This is the radius enclosing a mean cluster density equivalent to 500 times the critical density.

From the virtual X-ray observations the average temperature of the cluster was determined. The results were compared to the emission-weighted temperatures and spectroscopic-like temperatures obtained from the simulations. It was found that the fit of a single temperature model to the observed X-ray spectrum leads to a discrepancy between the emission-weighted temperatures and the observed average temperatures of up to 50%. It was observed that the spectroscopic-like temperature is systematically lower than the emission-weighted temperature and that the difference between the two temperatures is larger if the cluster presents high thermal complexity, agreeing with [60, 61, 62].

For the most massive cluster in our sample, a highly thermally inhomogeneous intracluster medium was identified. The mismatch between the emission-weighted temperature and the spectroscopic-like temperature is of 35% for this cluster. The emission-weighted temperature overestimates the observed average temperature while the spectroscopic-like

temperature reproduces it within the error bars.

To perform the fitting of a model to the observed spectrum, the lower energy part of the spectrum was discarded in order to to check if it would improve the agreement between the observed temperatures and the emission-weighted temperatures. A mild trend that the energy cut in the photon spectrum appears to be dependent on the cluster mass was found, but analysis of a larger cluster sample is necessary to determine this dependence.

The X-ray images were used to extract the X-ray surface brightness profile of each data set. A single β model was fitted to the observed brightness profiles providing the necessary parameters to determine the density profiles of the clusters. For our sample, the X-ray surface brightness profiles are generally well fitted by the β model if the most inner part of the cluster is excluded.

The total masses of the clusters were calculated using the fitted temperatures and the density profiles obtained from the β model fit. For that it was assumed hydrostatic equilibrium, spherical symmetry and isothermality of the intra-cluster medium.

The results indicate that the values of the clusters masses computed by assuming hydrostatic equilibrium are dependent on the temperature profiles. The assumption of isothermality leads to errors in the mass determination of up to 43%, showing that the temperature profiles are necessary in deriving the cluster mass using the hydrostatic equilibrium equation.

Other sources of error in the mass determination can come from departure of hydrostatic equilibrium [9]. Simulations by [68] suggest that hydrostatic equilibrium assumption underestimates the total cluster mass. It is observed a underestimation of the cluster mass for the most massive cluster.

The errors associated to the temperature are also relevant. These are related to the spectral fit, including the uncertainties in the instrumental calibration. The total cluster mass derived from the hydrostatic equilibrium assumption is proportional to the temperature, in this way errors in the temperature would translate into errors in the total cluster mass.

The gas masses of each cluster were calculated by integrating the density profiles over the volume of the cluster. For the most massive cluster, the gas masses derived from the X-ray observation and the simulated gas mass, agree better than the observed total mass and real mass. This better agreement may come from the fact that the temperature profile is not needed in the determination of the gas mass.

With the computed clusters total masses and observed temperatures it was possible to investigate the relation between these two quantities. A power law model of the form $M = A\,(kT/1keV)^{\alpha}$ was fitted to the mass-temperature relation.

The best fit parameters obtained are $\alpha = 1.74 \pm 0.04$ and $A = (2.47 \pm 0.32) \times 10^{13} M_{\odot}$. The slope obtained in this analysis is steeper than the expected value of $\alpha = 1.5$ predicted by the self-similar model based on gravitation. However, it is consistent with previous work done by [9, 39, 40, 69] with samples including low temperature clusters ($kT \leq 3$ keV). The scatter in the mass estimation with respect to the simulated mass is found to be $\sigma_{mass} = 0.36$ and the scatter in the mass-temperature relation is $\sigma_{m-t} = 0.22$.

Adding the results obtained in this thesis to previous studies on scaling relations, we find

that a definitive value of the slope of the mass-temperature relation is still undetermined and dependent on extensive studies of large unbiased samples in order to clarify how the mass scales with the temperature. The high value of α may suggest the gravitational collapse is not the only process governing the heating of the gas trapped in the cluster potential well [70].

An important remark is that the mass-temperature relation depends on how well the total mass of the clusters can be constrained, and also on how the average cluster temperature is defined, since the intra-cluster medium is not isothermal. In this project the temperature profiles were not consider when calculating the total cluster mass using the hydrostatic equilibrium assumption, and the temperatures were derived by fitting a model to the entire X-ray spectrum within radius R_{500}.

The temperature profiles would interfere significantly in the total cluster mass for systems presenting high thermal inhomogeneity, as is the case for the most massive cluster in our sample. The core of the clusters could also have been excluded and a thermal model fitting to the coreless X-ray spectra would exclude the thermal complexity that cool flows in the inner part of the cluster create. That could have an impact in the average temperature value. The errors coming from the temperature will produce errors in the value of the cluster total mass, however, they should not interfere in the results obtained for the mass-temperature relation.

The natural continuation of this work will be to extend the methods applied in this thesis to a larger sample of clusters. This will provide a more realistic and relevant statistical analysis and put better constraints on the scaling laws governing the mass-temperature relation.

For a larger sample, the virtual observations will be performed with longer exposure times in order to get enough resolution to derive temperature profiles and consider in this way the non-isothermality of the intra-cluster medium. Another step would be to add a more realistic background including particle background and point sources to also test for bias on the background subtractions.

Bibliography

[1] K. Pedersen & H. Dahle. *arXiv:astro-ph/0603260*, 2006.

[2] B. S. Ryden. *Introduction to Cosmology*. Addison Wesley, USA, 2003.

[3] G. M. Voit. *astro-ph/0410173*, 2004.

[4] Z. Haiman et al. *arXiv:astro-ph/0507013*, 2005.

[5] D. N. Spergel et al. *ApJ*, 170:377–408, 2007.

[6] S. Weinberg. *Gravitation and Cosmology*. Wiley, New York, USA, 1972.

[7] E. Hubble. *PNASUSA*, 15:3:168–173, 1929.

[8] S. Dodelson. *Introduction to Cosmology*. Academis Press, USA, 2003.

[9] M. Arnaud. *arXiv:astro-ph/0508159*, 2005.

[10] S. Borgani & L. Guzzo. *Nature*, 409:39–45, 2001.

[11] M. Arnaud et al. *Mem. S.A.It.*, 75:529, 2004.

[12] W.J. Kaufmann. *Universe*. W. H. Freeman and Company, New York, USA, 1991.

[13] C. R. Mullis et. al. *ApJ*, 623:L85–L88, 2005.

[14] P. Rosati et al. *ARA&A*, 40:539–577, 2002.

[15] Y. Mellier. *A&A*, 37:127–189, 1999.

[16] Kenneth S. Krane. *Introductory Nuclear Physics*. Wiley, USA, 1988.

[17] B. H. Bransden & C. J. Joachaim. *Physics of Atoms and Molecules*. Wiley, New York, USA, 1992.

[18] A. C. Fabian & S. W. Allen. *ISBN-981-238-580-0*, pages 197–2008, 2003.

[19] I. R. King. *ApJ*, 174:L123, 1972.

[20] A. Cavalieri & R. Fusco-Fermiano. *A & A*, 49:137, 1976.

[21] C. Jones & W. Forman. *ApJ*, 276:38–55, 1984.

[22] M. Roncarelli et al. *MNRAS*, 373:1339–1350, 2006.

[23] L. D. Ferramacho & A. Blanchard. *A&A*, 463:423–426, 2006.

[24] G. Pratt et al. *A&A*, 446:429–438, 2006.

[25] A. Kravtsov et al. *ApJ*, 625:588–598, 2005.

[26] Vikhlinin et al. *ApJ*, 640:710–715, 2006.

[27] M. L. Norman. *arXiv:astro-ph/0511451*, 2005.

[28] S. Borgani et al. *MNRAS*, 361, 2005.

[29] S. Borgani. *arXiv:astro-ph/0605575*, 2006.

[30] N. Kaiser. *MNRAS*, 222:323, 1986.

[31] N. Kaiser. *ApJ*, 383:104, 1991.

[32] A. E. Evrard & J. P. Henry. *ApJ*, 383:95, 1991.

[33] E. Pointecouteau. *A&A*, 435:1–7, 2005.

[34] Zhang et al. *A&A*, 467:437–457, 2007.

[35] M. Markevitch. *ApJ*, 504:27, 1998.

[36] M. Arnaud & A. E. Evrard. *MNRAS*, 305:631, 1999.

[37] T. H. Reiprich and H. Boehringer. *ApJ*, 567:716–740, 2002.

[38] R. Stanek et al. *ApJ*, 648:956–968, 2006.

[39] A. Finoguenov et al. *A&A*, 368:749–759, 2001.

[40] A. J. R. Sanderson et al. *MNRAS*, 340:989–1010, 2003.

[41] M. Arnaud et al. *A&A*, 441:893–903, 2005.

[42] M. Arnaud et al. *A&A*, 389:1, 2002.

[43] S. W. Allen. *arXiv:0706.0033v1[astro-ph]*, 2007.

[44] Fabian et al. *MNRAS*, 32:L20–L24, 2001.

[45] Rosati et al. *ApJ*, 127:230–238, 2004.

[46] Valtchanov et al. *A&A*, 423:75–85, 2004.

[47] *XMM-Newton User's Handbook - Issue 2.2*. ESA, 2004.

[48] de Chambure et al. Xmm's x-ray telescopes. *ESA bulletin 100*, 1999.

[49] S. Borgani et al. *MNRAS*, 367:1641–1654, 2006.

[50] D. Nagai et al. *arXiv:astro-ph/0611013*, 2006.

[51] S. Borgani et al. *MNRAS*, 348:1078–1096, 2004.

[52] Springel et al. *New Astronomy*, 6:79–117, 2001.

[53] C. Hededal et al. *in preparation*, 2007.

[54] SciSim Team. *SciSim User Guide 4.0*. SciSim Team, 2005.

[55] Steve Snowden et. al. *The XMM-Newton ABC Guide*. NASA/GSFC, 2003.

[56] Fabian et al. *A&A*, MNRAS:779, 1994.

[57] Vikhlinin et al. *ApJ*, 525:47–57, 1999.

[58] Keith Arnaud & Ben Dorman. *Xspec User Guide for version 11.3.x*. Nasa/GSFC, 2003.

[59] H. Kawahara et al. *arXiv:astro-ph/0611018*, 2006.

[60] P. Mazzotta et al. *MNRAS*, 354:10–24, 2004.

[61] E. Rasia et al. *ApJ*, 618:L1–L4, 2005.

[62] B. Mathiesen & A. Evrard. *ApJ*, 546:100–116, 2001.

[63] E. Rasia et al. *MNRAS*, 369:2013–2024, 2006.

[64] J. H. Croston. *A & A*, 459:1007–1019, 2006.

[65] E. Pointecouteau. *Advances in Space Research*, 36:659–662, 2005.

[66] S. W. Allen et al. *MNRAS*, 328:L37, 2001.

[67] Vikhlinin et al. *ApJ*, 628:655–672, 2005.

[68] S. Ettori et al. *A&A*, 391:841–855, 2002.

[69] Kay et al. *MNRAS*, 355:1091–1104, 2004.

[70] S. Ettori et al. *A&A*, 417:13–27, 2004.